Atmospheric Research 325 (2025) 108236

Contents lists available at ScienceDirect

Atmospheric Research

journal homepage: www.elsevier.com/locate/atmosres

Quantifying turbulent coarse particle transport over drylands of Southeastern Iberia using a stand-alone Doppler lidar methodology

Jesús Abril-Gago [a,b], Pablo Ortiz-Amezcua [a,b], Andrew S. Kowalski [a,b], Juan Antonio Bravo-Aranda [a,b], María José Granados-Muñoz [a,b], Juana Andújar-Maqueda [a,b], Lucas Alados-Arboledas [a,b], Juan Luis Guerrero-Rascado [a,b,*]

[a] *Andalusian Institute for Earth System Research (IISTA-CEAMA), University of Granada, Granada, Spain*
[b] *Department of Applied Physics, University of Granada, Granada, Spain*

ARTICLE INFO

Keywords:
Aerosol particles
Particle fluxes
Doppler lidar
Drylands
Particle emissions

ABSTRACT

Using a methodology for the estimation of coarse particle exchanges via Doppler lidar, based on the eddy covariance technique, profiles of vertical transport velocities were derived and analyzed. The methodology was tested across diverse atmospheric conditions in two different Mediterranean dryland landscapes in Southeastern Spain, namely Guadiana-UGR (extensive, inland olive grove), and Aguamarga (shrubland with maritime influence). Firstly, study cases were analyzed and the main atmospheric mechanisms impacting particle transport were identified. Convective mixing within the boundary layer was found to be the primary driver of the upward particle transport. However, cloud cover was observed to attenuate the transport velocity, while significant deposition events were observed during a Saharan dust outbreak. Secondly, positive transport velocities were found during convective periods and lower, yet positive, values during non-convective periods. Higher transport velocities were observed during a drier period at Guadiana-UGR, likely due to drier soil conditions. Aguamarga exhibited notably lower transport velocities. Considering only the lowermost observational level (105 m above the ground), net emission of particles was observed. Footprint analysis supported the representativeness of the fluxes. Our findings provide novel insights into particle exchanges over Mediterranean drylands, quantifying the turbulent transport and identifying its atmospheric drivers. Additionally, the considered ecosystems were found to be net sources of particles during the study periods. These results highlight the role of drylands as emerging contributors to global dust emissions in the context of climate change.

1. Introduction

Drylands are regions with low average annual rainfall and high potential evaporation rates, due to aridity and high temperatures, encompassing deserts, semiarid regions and dry steppes. They represent between 45 and 47 % of global land area across different continents (Mirzabaev et al., 2022) and are naturally vulnerable ecosystems due to their particular climate conditions. The current context of climate change poses risks to their sustainability (Ali et al., 2022; Mirzabaev et al., 2022; Abel et al., 2023; Eljamassi et al., 2023). The study of these ecosystems, their processes, feedbacks and interactions is fundamental to understand and evaluate their degree of vulnerability.

Notable trends of dryland expansion have been observed with 44.5 % of global area becoming dryer in the last two decades (Abel et al., 2023), and 6 % of drylands undergoing desertification in recent decades, while dryland area is projected to expand by ~10 % by 2100 (Mirzabaev et al., 2022). Drylands were estimated to encompass 69 % of Spain in 2011 (Zdruli, 2011), and the Mediterranean region has been drying out during recent decades (Ali et al., 2022). Recent studies on the Iberian Peninsula indicate a substantial projected increase in the intensity, frequency and duration of drought during the current century, leading to an increase in aridity (García-Valdecasas Ojeda et al., 2021a,b; Spinoni et al., 2018).

Ecosystems exchange energy and matter, including sensible heat and trace gases. The eddy covariance (EC) technique has been traditionally applied to characterize these vertical exchanges (e.g., Aubinet et al., 1999). The technique is based on the fact that the covariance of a scalar (a) with the vertical wind speed fluctuations provides the kinematic turbulent flux density of that scalar, i.e.:

* Corresponding author at: Instituto Interuniversitario de Investigación del Sistema Tierra en Andalucía, Avenida del Mediterráneo, s/n, 18006 Granada, Spain.
E-mail address: rascado@ugr.es (J.L. Guerrero-Rascado).

https://doi.org/10.1016/j.atmosres.2025.108236
Received 25 January 2025; Received in revised form 8 April 2025; Accepted 21 May 2025
Available online 24 May 2025

$$F_a = \rho\, \overline{a'w'} \quad (1)$$

where F_a is the flux density (or "flux"; Kowalski, 2023), ρ the air density, a' the fluctuation of a about its mean (typically a 30-min average) and w' the fluctuation of the vertical wind speed w about the mean (Stull, 1988). In practice, an ultrasonic anemometer is synchronized with a fast-response sensor of the desired magnitude, a gas analyzer, and installed atop towers of different heights (e.g., Hari et al., 2013; Serrano-Ortiz et al., 2020; Aranda-Barranco et al., 2023), measuring the ambient air.

Ecosystems also exchange particles, dependent on wind dynamics, surface roughness, vegetation and soil surface conditions (Ishizuka et al., 2008; Webb et al., 2021). The study of dust emissions and sinks has gained increasing attention in recent decades (e.g., IPCC, 2001, 2007, 2013, 2021). Climate change is an important driver of dust emission changes (Mirzabaev et al., 2022; Tegen and Schepanski, 2018) and is expected to increase soil erosion in semiarid regions (Ali et al., 2022). Additionally, semiarid land degradation and drying of water bodies will likely contribute to higher dust activity (Mirzabaev et al., 2019, 2022), which is particularly important as particle emissions can change atmospheric composition and impact ecosystems far from the source. However, the low accuracy in the determination of present anthropogenic dust emissions limits the reliability of future projections of dust emissions (Webb and Pierre, 2018). Nevertheless, higher future dust emissions are consistent with climate change projections (Mirzabaev et al., 2022; Allen et al., 2016), while new sources for dust emissions may appear with climate change (Bhattachan et al., 2012; Bhattachan and D'Odorico, 2014).

Particle turbulent exchanges have been frequently characterized and quantified over a wide range of ecosystems, surfaces and conditions (e.g., Gallagher et al., 1997; Pryor et al., 2007; Casquero-Vera et al., 2022), nearly always using in-situ instrumentation, namely a particle counter and a sonic anemometer. Since the first application of EC to the study of particle exchanges (Wesely et al., 1977), the technique has been standardized, improved and reviewed (Pryor et al., 2008). Nevertheless, turbulent particle exchanges over semiarid ecosystems have received relatively limited attention (e.g., Lamaud et al., 1994; Webb et al., 2021; Fernandes et al., 2023).

Remote sensing instrumentation has been widely used to study atmospheric particles, characterize their optical and microphysical properties, quantify their presence and analyze the processes they impact (e.g., Abril-Gago et al., 2022; López-Cayuela et al., 2023; Salgueiro et al., 2023; Gidarakou et al., 2024). Lidar technology has occasionally been used to investigate turbulent exchanges of trace gases and latent heat (e.g., Senff et al., 1994; Giez et al., 1999; Gibert et al., 2011), providing vertically resolved turbulent exchanges (i.e., vertical profiles), in contrast to conventional, single-height EC measurements. However, the application of lidars to particle exchange characterization has not been studied in depth. Engelmann et al. (2008) presented the first study addressing particle fluxes combining Raman and Doppler lidars. However, that study presented the methodology and just a case study under very specific conditions. Wang et al. (2021) carried out an analogous study with a coherent Doppler lidar and a sun-photometer, also for specific atmospheric conditions. A recent approach presented by Petters et al. (2024) pioneered a methodology employing Doppler lidars, calibrated with optical particle counters and radiosondes, to retrieve backscatter and particle number concentration fluxes within the lidar's lower observational level. The study disclosed the promising potential of Doppler lidars in the determination of particle emissions of ecosystems.

This study aims to characterize the daily patterns of turbulent particle transport at two distinct locations in Southern Spain and to identify its main drivers, applying a stand-alone methodology for assessing particle exchanges using Doppler lidar measurements. This methodology has been applied across different meteorological and climatological conditions during three different field campaigns: BLOOM and BLOOM II (turBulence and oLea pOllen prOperties experiMent), and SCARCE (Synchronized Characterization of Aerosol, Radon and Carbon dioxide Exchanges in drylands). This study is structured as follows: Sect. 2 presents the instrumentation and the field campaigns; Sect. 3 is devoted to the methodology applied to derive particle flux profiles; Sect. 4 presents the analysis and discussion of the campaigns and several case studies used to test the method under different conditions; and, finally, Sect. 5 states the most relevant findings of the study.

2. Experimental sites and instrumentation

2.1. The stations

The rural, inland station of Guadiana-UGR (37.91°N, 3.23°W, 370 m asl) is located within an extensive traditional olive grove in Southern Spain, predominantly composed of *Olea europaea*, the common olive tree, and spontaneous ground vegetation. Olive groves dominate the region's agricultural landscape, covering hundreds of hectares of terrain around the station and creating a relatively homogeneous landscape. Úbeda, a city of around 34,600 population, is the closest significant population center, located 16 km northwest. The station itself is located in a fairly flat area, surrounded by few hills of less than 600 m asl within a 10-km radius, and distant mountains: Sierra de Cazorla (2107 m asl) is about 35 km east and Sierra Mágina (2167 m asl) about 25 km southwest. The climate zone is Mediterranean, Csa Köppen classification (El-Kenawy et al., 2022), characterized by hot, dry summers and mild, wet winters. More station information was given by Chamizo et al. (2017) and Aguirre-Garcia et al. (2021), with atmospheric dynamics addressed by Ortiz-Amezcua et al. (2022b).

The rural station of Aguamarga (36.94°N, 2.03°W, 205 m asl) is positioned near the heart of Cabo de Gata-Níjar Natural Park, near the Southeastern coast of Spain, a region of Mediterranean scrub ecosystems of exceptional ecological significance. Campohermoso is the closest significant population center, located almost 10 km west, with around 8000 inhabitants. The Mediterranean coast is 6 km away from the station. The landscape is dotted with small hills of no more than 400 m with divers, sparse vegetation species naturally adapted to severe water stress, chiefly *Machrochloa tenacissima* (Alados et al., 2003). Furthermore, the region is dotted with vegetable greenhouses. This is the most arid region of Spain, BSh Köppen classification (El-Kenawy et al., 2022), with an average precipitation of 160 mm per year (Capel Molina, 1995). Further insight into the experimental site (referred to by its alias, Balsa Blanca) is provided by López-Ballesteros et al. (2018) and Moya et al. (2019).

Atmospheric aerosol composition in these stations depends both on local emissions and advection from other regions. Dust intrusions are the most significant particle inputs over the Southeastern Iberian Peninsula, a hotspot with frequent Saharan dust outbreaks (e.g., Papanikolaou et al., 2024; López-Cayuela et al., 2023; Guerrero-Rascado et al., 2008, 2009; Bravo-Aranda et al., 2015; Granados-Muñoz et al., 2016; Mandija et al., 2016), arriving both in the free stratosphere and within the atmospheric boundary layer (ABL). These intrusions transport significant particle loads that settle through dry or wet deposition and influence soil composition (Molinero-García et al., 2022).

2.2. Instrumentation and campaigns

Particle transport measurements were carried out with a single atmospheric instrument: the HALO Photonics StreamLine Doppler lidar, included within AGORA (the Andalusian Global ObseRvatory of the Atmosphere). Managed by the GFAT (Atmospheric Physics Group) of the University of Granada, the instrument emits 1565 nm laser radiation at 15 kHz and with a heterodyne detector identifies the Doppler shift of the backscattered signal caused by atmospheric constituents. This information is then processed by the standardized software package 'HALO lidar toolbox', developed by Manninen (2019), in order to retrieve various products such as 3D wind fields or wind shear within the ABL, at a minimum height of 90 m above ground (effective full-overlap height) with a vertical resolution of 30 m. The Doppler lidar was primarily configured to measure in stare mode, with its beam directed vertically by default. Additionally, it conducted Vertical-Azimuth-Display (VAD) scans every 10 min at 75° elevation, each lasting approximately 1.2 min. As a result, VAD scans account for an estimated 3.6-min loss of stare data per 30-min interval. The scan configuration was based on the approach used by Manninen et al. (2018), balancing the acquisition of vertical, horizontal and turbulence information of the atmosphere. The standard temporal resolution of the products is set at 3 min. A more detailed description of the instrument and the configured scans is given by Ortiz-Amezcua et al., 2022b. Thus, Doppler lidar systems allow, for example, the study of wind and turbulence patterns within the ABL (e.g., Ortiz-Amezcua et al., 2022a, 2022b) and to carry out satellite calibration and validation activities (e.g., Abril-Gago et al., 2023).

The instrument was located at the stations mentioned in Sect. 2.1 during dedicated campaigns: BLOOM (18 May to 21 June 2022, Guadiana-UGR), BLOOM II (28 March to 31 May 2023, Guadiana-UGR) and SCARCE (18 July 2023 to 15 January 2024, Aguamarga). During campaigns, the Doppler lidar was co-located with a CHM15k-Nimbus ceilometer (Lufft, Germany) integrated in ICENET (Iberian CEilometer NETwork; Cazorla et al., 2017) and a sun–sky photometer (Cimel Electronique, France) integrated in AERONET (AErosol RObotic NETwork; Holben et al., 1998), facilitating the characterization of the atmosphere and interpretation of the observed particle emission/deposition. Additionally, volumetric soil water content (VWC, in $m^3\ m^{-3}$) data from a CS616 (Campbell Scientific, United States of America) sensors permanently installed at a depth of 10 cm at the station were used to quantify the soil humidity during the campaigns. A CR3000 (Campbell Scientific) data logger registered measurements and recorded 30-min averages.

2.3. Wind and aerosol products

Products from the Doppler lidar, the main instrument used in the current study, were obtained by the 'HALO lidar toolbox' with the different scans. Vertical profiles of attenuated backscatter coefficient, $\beta_{att}(z)$, and vertical air velocity, $w(z)$, were retrieved with the stare measurements at 1 Hz. While w is a direct product, β_{att} needs to be retrieved from the calibrated signal. To this end, the artifacts described by Manninen et al. (2016) and Vakkari et al. (2019) were firstly corrected and the signal is then calibrated with the focus function as described by Pentikäinen et al. (2020). Doppler lidar products underwent filtering based on the signal-to-noise ratio (SNR) of the lidar signal. Height intervals, or bins, with a SNR less than 0.006 (− 22.2 dB) were filtered out (Manninen et al., 2016, 2018). These profiles were later used to apply the EC technique in order to obtain the vertical transport velocities, as presented in Sect. 3.1. Additional products were obtained for further atmospheric characterization, namely the horizontal wind speed and direction, the turbulence source classification and the specific Turbulent Kinetic Energy (TKE) dissipation rate (ε; O'Connor et al., 2010). The horizontal wind speed and direction profiles were retrieved from the VAD scans. The turbulence source classification (Manninen et al., 2018) classified the mechanism mostly responsible for turbulence at a given altitude, generally within the ABL. This product was obtained from the combination of stare and VAD scans, although they were provided in 3-min profiles, keeping the original vertical resolution. Ultimately, profiles of ε represent the rate at which TKE dissipates into internal thermal energy. High values of ε, exceeding the threshold of $10^{-4}\ m^2\ s^{-3}$, represent moments of high turbulence activity (e.g., Andújar-Maqueda et al., 2025 O'Connor et al., 2010; Andújar-Maqueda et al., 2025) associated with surface-related convection (Manninen et al., 2018), while lower values indicate stability and stratification within the atmosphere.

AERONET sun-sky photometer products (Version 3) furthered understanding of the particles present in the atmospheric column over the station. Level 2 direct Sun products of aerosol optical depth at 500 nm (AOD_{500}), Ångström exponent calculated in the spectral range between 440 and 870 nm channels ($AE_{440–870}$) and fine-mode-fraction at 500 nm (FMF_{500}) provided information about the amount and size of the particles. Level 1.5 size distribution and multispectral single-scattering albedo (SSA) products of the inversion algorithm (Dubovik et al., 2002) identified the predominant size mode and classified aerosol type. However, AERONET inversions under low aerosol loads (AOD_{440} lower than 0.40) were not used (Dubovik et al., 2006; Shin et al., 2019). Level 1.5 direct Sun products substituted when level 2 products were not available. The ceilometer's range-corrected signal (RCS) at 1064 nm overviewed the atmospheric components present over the station and estimated the atmospheric boundary layer height (ABLH) and mixing layer height (MLH) via STRATfinder (Kotthaus et al., 2020). The standardized algorithm created a weight field (one weight for each altitude and time step), combining the variance (e.g., Poltera et al., 2017) and gradient methods (e.g., de Bruine et al., 2017). The minimum-weight path identified layer boundaries. Additionally, the algorithm estimated cloud base height, used to filter ABLH and MLH data when they coincided with the cloud base, avoiding potential biases in the statistics. The Navy Aerosol Analysis and Prediction System (NAAPS; Westphal et al., 2009) and the Barcelona Supercomputing Center–Dust REgional Atmospheric Model (BSC-DREAM8b; Basart et al., 2012) forecasts were consulted in order to assess the presence of advected dust or smoke particles in the region.

3. Methodology

The methodology was based on that presented by Engelmann et al. (2008), adapted for a stand-alone approach based on Doppler lidar. Using this single instrument introduced the advantages of automatization and simplification of the EC technique application. Additionally, as both $\beta_{att}(z)$ and $w(z)$ were obtained with the same instrument, avoiding errors caused by instrument separation (Kristensen et al., 1997). However, the obtention of particle mass fluxes was excluded and a proxy to these fluxes was obtained.

3.1. Vertical transport velocity

The attenuated backscatter coefficient is defined as:

$$\beta_{att}(z) = \beta(z)\ T^2(z) \tag{2}$$

where $\beta(z)$ is the volume backscatter coefficient at an altitude z and T represents the atmosphere's vertical transmittance of radiation between the instrument and z. The backscatter coefficient describes how much light is scattered into the backward direction (Wandinger, 2005) and is given by:

$$\beta(z) = \sum\nolimits_i N_i(z)\ \frac{d\sigma_i(\pi)}{d\Omega} \tag{3}$$

where i indicates the different type of scatterer, N_i the concentration of scatterers of type i and $d\sigma_i/d\Omega$ the differential scattering cross section in the backward direction (π) of type i. Thus, $\beta(z)$, and consequently $\beta_{att}(z)$, represents an optical property of the atmospheric constituents responsible for backscattering lidar radiation. These coefficients are directly related to the number of particles and strongly influenced by their microphysical features, such as the scattering cross section, which in turn depends on the scatterers' size and geometry. However, $\beta_{att}(z)$ also encompasses the effects of the atmospheric transmittance, which should be removed.

The procedure for deriving $\beta(z)$ from lidar signals is standardized for conventional lidar systems (Klett, 1981; Fernald, 1984). However, due to instrumental and signal limitations, retrieving the Doppler lidar signal is not feasible with the desired time resolution for flux calculation. A different methodology, described by Baars et al. (2017), was employed to retrieve the so-called quasi-backscatter coefficient, $\beta_{quasi}(z)$, from

$\beta_{att}(z)$. If the procedure was convergent, then $\beta_{quasi}(z)$ should equal $\beta(z)$. Under the assumption of a standard lidar ratio of 55 sr (Baars et al., 2017) at 1565 nm, $\beta_{quasi}(z)$ was first retrieved from $\beta_{att}(z)$ and later used to compute particulate transport. To ensure analytical robustness, sensitivity examinations were conducted on the selection of the lidar ratio (ranging from 10 to 100 sr at 1565 nm), revealing a modest 3 % variance in calculated exchanges between extreme lidar ratio values.

The EC technique defines the turbulent flux density, commonly termed "flux" in the literature (Kowalski, 2023), as the covariance of the fluctuations of a variable, such as $\beta_{quasi}(z)$, and $w(z)$ (Stull, 1988), typically calculated over a 30-min averaging period. Thus, the vertical turbulent flux density of $\beta_{quasi}(z)$ is given by Eq. (1) as:

$$F_{\beta_{att}}(z) = \overline{\beta'_{quasi} w'}(z) \tag{4}$$

where $\beta'_{quasi}(z)$ and $w'(z)$ are calculated with the original resolution of 30 m and 1 s. $\beta'_{quasi}(z)$ represents fluctuations of $\beta_{quasi}(z)$, which correspond to fluctuations in particle number concentration (Petters et al., 2024), as microphysical properties vary negligibly compared to particle number concentration (Pal et al., 2010). Among atmospheric constituents, the 1565 nm Doppler lidar signal is particularly sensitive to coarse particles, enabling the retrieval of particle number fluxes of particles larger than 0.53 μm (Petters et al., 2024). The calculation of the flux density of $\beta_{quasi}(z)$ is possible utilizing the software created by Ortiz-Amezcua (2023). However, this flux density is provided in intricate units, namely in $sr^{-1}\,s^{-1}$. For this and other reasons, it is common to express exchanges in terms of deposition velocities (Chamberlain and Chadwick, 1953; Gallagher et al., 1997; Pryor, 2006), v_d, as:

$$v_d(z) = -\frac{\overline{\beta'_{quasi} w'}(z)}{\overline{\beta_{quasi}}(z)} \tag{5}$$

defined downward (hence the minus sign), in m s^{-1}. Considering the micrometeorological convention, positive values of v_d indicate downward transport of particles (deposition), while negative values represent upward transport (emission). However, for convenience, this study focuses on the vertical transport velocity, v_t, with spatial and temporal resolutions of 30 m and 30 min, respectively, given by:

$$v_t(z) = \frac{\overline{\beta'_{quasi} w'}(z)}{\overline{\beta_{quasi}}(z)} \tag{6}$$

The notation of the altitude z, included in the previous definition to make clear that profiles of v_t are obtained, will be omitted in the following text. Positive values of v_t imply net upward particle transport, while negative values indicate net downward transport. Additionally, v_t represents the vertical exchanges of particulate matter due to turbulent processes and should not be misinterpreted as vertical wind speed, which represents the average vertical motion of air. An analogous definition has been used occasionally in the literature to describe emission velocity, v_e (e.g., Dorsey et al., 2002; Longley et al., 2004). This definition has typically been applied to measurements near the surface, where the concept of particle *emission* (from the surface to the atmosphere) is clear. However, applying this concept at higher altitudes can be confusing. For instance, if a positive v_t is measured at 1 km, it would be wrong to conclude that the atmosphere at that altitude is *emitting* particles. Therefore, for clarity and consistency, this manuscript adopted a more general nomenclature, in terms of upward and downward *transport*. The usage of v_t (and its analogous v_d or v_e) facilitates the interpretation of the results and enables the comparison across different sites (Farmer et al., 2021).

Processing of particle fluxes measured with in-situ instrumentation, prior to the retrieval of the final products, is roughly standardized although some well-known corrections or statistical processing are not established as mandatory. Webb corrections (sometimes known as WPL) rectify the variation in particle concentrations induced by fluxes of heat and water vapor (Webb et al., 1980). Other corrections address the measured turbulent fluxes biases induced by the deliquescence of particles due to humidity (Kowalski, 2001). However, these corrections are not approachable with the current instrumentation, nor there is a consensus about the necessity of their application (e.g., Pryor et al., 2007; Järvi et al., 2009). The case of the WPL corrections, of the order of 1 mm s^{-1} (Webb et al., 1980), was expected to produce a small impact on the fluxes of particles (Pryor et al., 2017; Deventer et al., 2018), compared to the transport velocities obtained in the study (~10 mm s^{-1}), unlike for some trace gas fluxes. The present study did not take these corrections into account in the processing of the final particle fluxes. On the other hand, while statistical detrending of the covariances is sometimes employed, a consensus on its application remains elusive (Kowalski and Abril-Gago, 2025). Regarding the different filtering methods available, a simple linear detrending of the covariances is sufficient and recommended (Donateo et al., 2017; Pappaccogli et al., 2022; Petters et al., 2024). This approach would help in the interpretation of the fluxes, minimizing potential artifacts introduced by background trends (advection of aerosol particle layers) or sensor drifts (Gash and Culf, 1996). Following the methodologies established by previous studies (Engelmann et al., 2008; Petters et al., 2024), linear detrending of β_{quasi} and w was performed in this study.

3.2. Spectral analysis and stationarity test

Spectral analyses are regularly incorporated into eddy-covariance studies for quality assurance to determine the system's frequency response, gain insight into the nature of turbulence by decomposing turbulent parameters into their frequency components, and ultimately assess the reliability of the calculated turbulent fluxes. According to Kolmogorov's theory (Kolmogorov, 1941), for homogeneous and isotropic turbulence the energy spectra of turbulent parameters (e.g. w fluctuations) show how larger eddies transmit energy without dissipation to the smaller eddies, following a $-5/3$ power law in a part of the spectrum known as inertial subrange. The low-frequency subrange is dominated by the largest eddies, which are influenced by local structures (Kaimal et al., 1972), while the highest frequencies are largely affected by noise introduced by the setup design. When the energy spectral function, or power spectral density function, aligns with Kolmogorov's hypothesis, turbulence can be assumed to be properly developed, suggesting that the calculated turbulent fluxes are reliable. According to O'Connor et al. (2010), the Doppler lidar signal followed Kolmogorov's hypothesis within the convective boundary layer. However, caution should be exercised for other conditions. For example, recent turbulence theories (Goto and Vassilicos, 2016; Steiros, 2022; Wacławczyk, 2021) and observations (Karasewicz et al., 2024; Wacławczyk et al., 2022) demonstrate that during non-equilibrium transitions (e.g. immediately after sunset) energy spectra may exhibit deviations from $-5/3$ slope that are still compatible with turbulence presence. In the current study, a spectral analysis was carried out for two different scenarios and altitudes to evaluate whether a sufficient portion of the spectra falls accordingly in the inertial subrange, ensuring the derived turbulent fluxes were reliable for those conditions.

Since flux estimations were calculated in 30-min intervals, a stationarity test was carried out to determine if the covariance kept steady within the interval (Foken and Wichura, 1996). These changes may result from abrupt variations in the measured component or shifts in the weather patterns, which should not be interpreted as turbulent exchanges. The methodology proposed by Foken and Wichura (1996) was used and the covariances for each 5 min within each 30 min were calculated (6 intervals). After this, the 6 intervals were averaged into the same 30-min division of the flux calculations. Analogous 30-min covariances with differences larger than 60 % (Casquero-Vera et al., 2022) were considered non-stationary and were consequently omitted from the analysis.

3.3. Flux footprint analysis

The representativity of the fluxes were assessed through a flux footprint analysis. This estimates the source area surrounding the instrument that contributes to the measured vertical turbulent fluxes (Schuepp et al., 1990), i.e., the possible origin of the fluxes captured by the instrument. The higher the altitude of the measurement, the larger the footprint, and consequently the lesser the influence of the nearby ecosystem, unless the landscape is homogeneous and large enough. Additionally, the size and location of the source area also depends on surface features, like roughness, and meteorological conditions like wind direction and stability (Schmid, 1997). The assessment of the representativity of the sampled turbulent fluxes is a mayor challenge (Chu et al., 2021), which has been largely addressed through flux footprint analysis for near-surface towers (e.g., Serrano-Ortiz et al., 2011; Sánchez-Cañete et al., 2016; Salgueiro et al., 2020) and occasionally calculated for tall towers (e.g., Straaten and Weber, 2021; Matthews and Schume, 2022; Casquero-Vera et al., 2022). However, few studies have addressed flux footprint analysis when calculating turbulent fluxes with a lidar at different altitudes (Cooper et al., 2003), although it has been highlighted as a fundamental analysis to comprehend the retrieved fluxes (Leclerc and Foken, 2014). A flux footprint analysis for different scenarios was carried out at the lowest altitude measured by the Doppler lidar, as it would be the most representative of the particle fluxes taking place in the studied ecosystems and landscapes. The flux footprint model described by Kljun et al. (2015) was used and the location of the maximum footprint contribution (i.e., the distance between the instrument and the maximum contribution of the captured fluxes) was calculated as:

$$x_{\max} = 0.87\, z_m \left(1 - \frac{z_m}{h}\right)^{-1} \frac{\overline{u}(z_m)}{u_*} k \tag{7}$$

where z_m is the height of the measurement, h is the ABLH, $\overline{u}(z_m)$ is the wind speed at the measurement height, u_* is the surface friction velocity (Chamizo et al., 2017; Aranda-Barranco et al., 2023) and $k = 0.4$ is the von Karman constant. The advantage of using this method over other calculations provided by Kljun et al. (2015) was that the mentioned variables were measured at the station, and no further bibliographic parametrizations or values (like the surface roughness length, z_0) were needed. h values were estimated with STRATfinder, while $\overline{u}(z_m)$ was directly measured by the Doppler lidar and u_* was measured by a collocated sonic anemometer at surface level. $x_{\max}$ values were calculated in 30-min intervals for two differentiated scenarios provided by the Doppler lidar's turbulence source classification scheme, namely convective and non-convective (including non-turbulent, wind shear and intermittent). The limitations indicated by Kljun et al. (2015) were fulfilled in the scenarios considered in this study. However, the condition $z_m/L \geq -15.5$ (Kljun et al., 2015), where L is the Obukhov length, may not be met at higher altitudes during very unstable regimes, when L is negative and tends to 0. The condition $20z_0 < z_m < h_e$, where h_e is the altitude of the boundary layer entrainment zone, is consistently met, as the products of this Doppler lidar are confined within the boundary layer.

4. Results and discussion

4.1. Meteorology during the campaigns

During the BLOOM campaign, out of 35 days from 18 May to 21 June 2022, mid-level cloud cover was observed at some moment on 14 days (40 % of the total), and low clouds were recorded on 3 days (9 %), according to ceilometer information. According to the ceilometer and the sun-photometer, 21 (89 %) days showed some kind of aerosol plumes, some of which could be identified as Saharan dust layers. The average ABLH for this period was 2.6 ± 0.7 km, while the MLH daily maximum was 2.1 ± 0.5 km reached at 15:00 UTC and the average MLH daily minimum was 0.5 ± 0.1 km at 07:30 UTC (Fig. 1a). The wind patterns of the campaign exhibited two main modes (Fig. 1b), one related to the day-time regime, with anabatic flow up the river valley towards the mountains, and another with nighttime, katabatic flow draining from the mountains.

Fig. 1c illustrates the precipitation recorded in a nearby Spanish National Meteorological Agency (AEMET) station, Jaén (station code 5270B), less than 50 km away, and its climate trend (1980–2023). The AEMET records were preferred to the records of the Guadiana-UGR pluviometer due to the larger series available. The hydrological year 2021/2022 (from 1 October 2021 to 30 September 2022) exhibited substantial precipitation during spring (especially March and April) which allowed the spontaneous weed cover to develop normally. However, no significant precipitation at Guadiana-UGR was registered since late April, resulting in an already dry soil by the beginning of BLOOM. In fact, the VWC at 10 cm was (0.007 ± 0.003) m^3 m^{-3}, which is remarkably small compared to the yearly mean (0.053 ± 0.059) m^3 m^{-3}.

During BLOOM II, spanning 65 days from 28 March to 31 May 2023, mid-level cloud cover was noted at some moment on 11 days (17 %), while low clouds were observed on 2 days (3 %), and a prolonged period of rainfall occurred during 13 (20 %), as indicated by ceilometer data. Aerosol plumes, including some identifiable as Saharan dust layers, were observed on 23 days (35 %) through ceilometer and sun-photometer readings. The average ABLH for this period was 2.1 ± 0.7 km, while the MLH mean maximum and minimum values were 1.7 ± 0.5 km reached at 15:00 UTC and 0.5 ± 0.1 km reached at 23:00 UTC.

The hydrological year 2022/2023 was characterized by a critical dry period. No precipitation was recorded from 9 March to 18 May 2023 (Fig. 1c), when most of the spontaneous weed cover usually develops at the station. This vegetation did not develop during that period of the campaign, leaving the soil highly exposed to erosion. Thus, BLOOM II was characterized by a severe precipitation deficit and consequent terrain aridity, with an average VWC at 10 cm of (0.003 ± 0.001) m^3 m^{-3}, which was considerably low compared to the annual mean of (0.064 ± 0.060) m^3 m^{-3}. Some precipitation occurred on 19 May 2023, which was followed by a 2-week intensive rainfall. Thus, in the following analysis of BLOOM II, a clear distinction will be made between these two periods: 28 March to 18 May 2023 (dry and arid soil) and 19 to 31 May 2023 (rain and moist soil). The wind roses for these two periods of BLOOM II (not shown here) were similar between them and similar to that of BLOOM.

During SCARCE, out of 182 days from 18 July 2023 to 15 January 2024, 24 days (13 %) showed mid-level cloud cover, 29 (16 %) significant low-cloud cover and 13 (7 %) days showed precipitation at some moment of the day. Additionally, 34 days exhibited significant aerosol layers over the station, coupled with or decoupled from the boundary layer. The marine boundary layer of the station showed little diurnal variation, as expected for near-shore locations (Fig. 2a). The average ABLH for this period was 1.0 ± 0.8 km, while the MLH daily maximum was 0.7 ± 0.3 km reached at 14:00 UTC and the minimum MLH was 0.4 ± 0.1 km at 23:00 UTC. The hydrological year 2022/2023 (Fig. 2c) precipitation records did not present any significant deviation with respect to the climate trend (1980–2023) of the AEMET station Almeria (6297), less than 30 km away. Accumulated precipitation of 68.1 mm was recorded during the campaign period, while the most significant precipitation record (almost 12 % of the annual precipitation) was registered between 2 and 3 September 2023. In the following analysis of SCARCE, the whole period was analyzed together, although cases with precipitation were filtered out. The wind rose (Fig. 2b) indicated two predominant modes aligned with the coast and related to the easterly and westerly wind regimes of the Alboran Sea (HMSO, 1962).

In summary, the last rainfall over Guadiana-UGR took place several weeks before BLOOM kicked off, with no significant rain recorded during the campaign. Thus, with the soil already dry by the beginning of

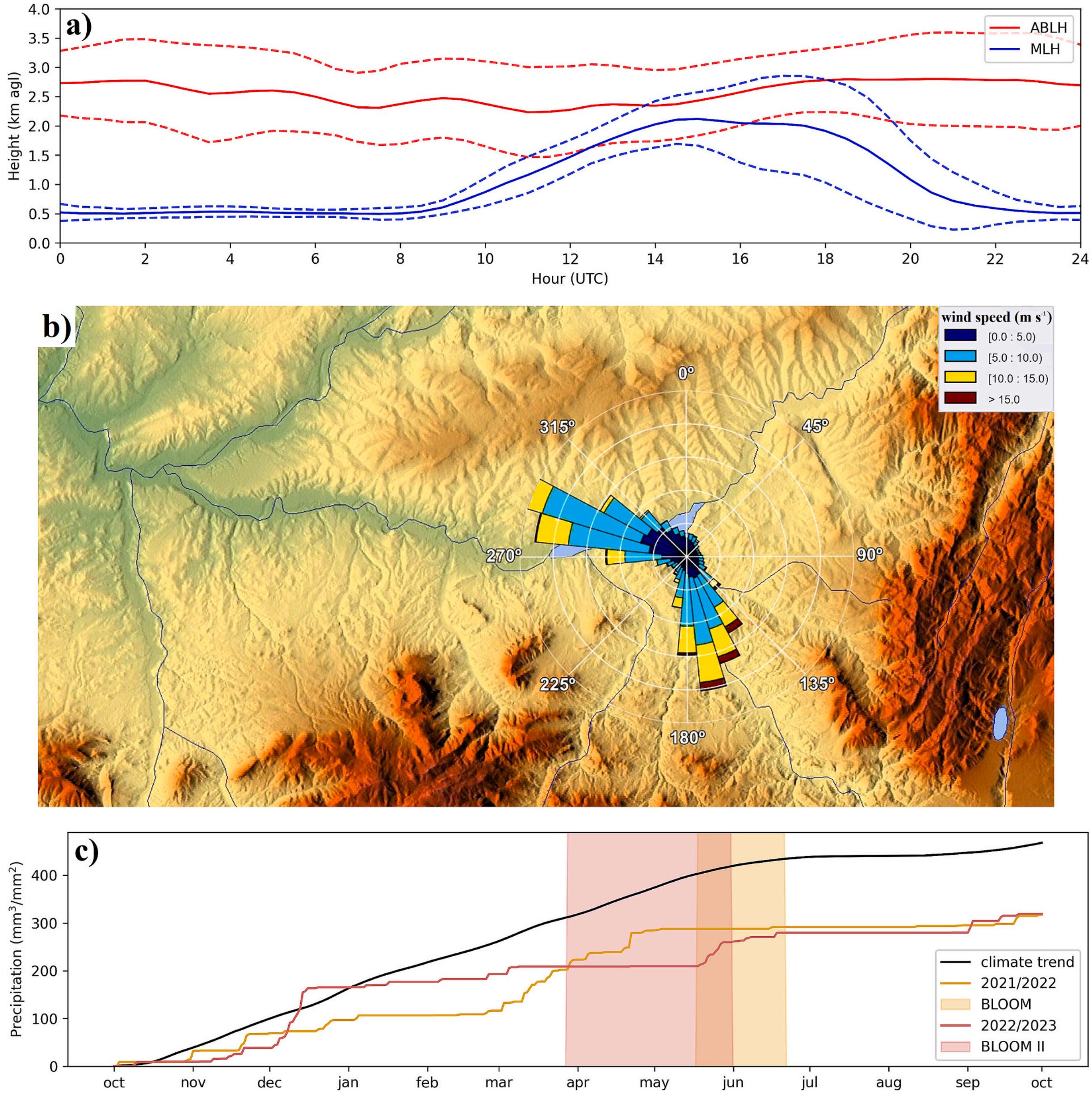

Fig. 1. a) Average ABLH and MLH patterns from 18 May to 21 June 2022 (BLOOM). Solid lines indicate the mean value, while dashed lines indicate the standard deviation. b) Wind rose from 18 May to 21 June 2022 (BLOOM) superimposed on a regional topographic map. The meteorological convention is used for the wind direction, i.e., direction indicates the origin of the wind. The colour scale indicates the horizontal wind speed in m s^{-1}. Map data: © OpenStreetMap contributors. c) Precipitation climate trend of the AEMET station Jaén (5270B), closest to our Guadiana-UGR station, and precipitation during hydrological years 2021/2022 and 2022/2023 of the same station. The periods of the BLOOM (2022) and BLOOM II (2023) campaigns are highlighted. (For interpretation of the references to colour in this figure legend, the reader is referred to the web version of this article.)

the campaign, soil conditions were assumed constant during the campaign and the whole period was studied at once. BLOOM II was characterized by an exceptionally dry hydrological year, which inhibited the spontaneous weed cover development and consequently exposed the soil to erosion. However, the two last weeks of BLOOM II were characterized by an intense rainfall. Due to the differences in the meteorological and soil conditions, the rainy period was excluded, and the whole dry period was studied at once. SCARCE was characterized by low precipitation records. In this case, cases with rain were excluded, and days with no precipitation were studied together. The decision to eliminate precipitation periods was consistent with the literature (e,g, Rannik et al., 2009; Masseroni et al., 2014; Petters et al., 2024), improving data quality and focusing on dry particle exchanges.

4.2. Spectral analysis and stationarity test

A spectral analysis of the Doppler lidar products was carried out to determine if the system frequency response is adequate and validate the flux retrieval according to different turbulence scenarios. Fig. 3 displays the power spectral densities of β_{att} and w for the period from 09:30 to 10:30 UTC (convective) and from 19:30 to 20:30 UTC (non-convective) of the 10 April 2023 (BLOOM II) at 105 and 495 m. The density functions of the convective period (Fig. 3a and b) fell within the inertial subrange as described by Kolmogorov, regardless of the sampling altitude. Noise in the sampled time series appears as a constant contribution to the spectra at high frequencies and is found at the highest investigated height for both β_{att} and w, and only for β_{att} at the lowest height. This result aligns with similar studies (Engelmann et al., 2008; O'Connor

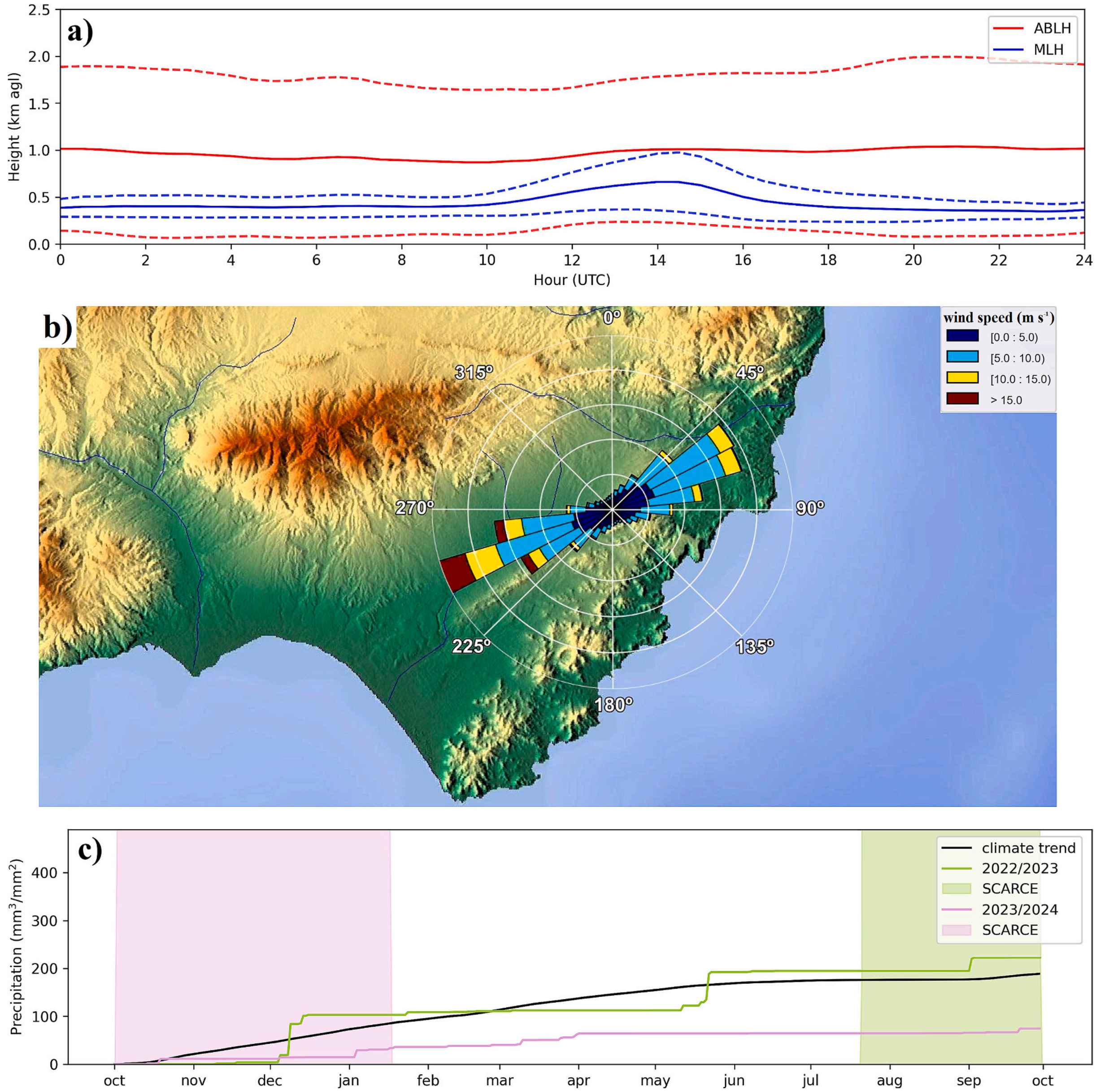

Fig. 2. a) Average ABLH and MLH pattern from 18 July 2023 to 15 January 2024 (SCARCE). Solid lines indicate the mean value, while dashed lines indicate the standard deviation. b) Wind rose from 18 July 2023 to 15 January 2024 (SCARCE) superimposed on a regional topographic map of the region. The meteorological convention is used for the wind direction, i.e., direction indicates the origin of the wind. The colour scale indicates the horizontal wind speed in m s^{-1}. Map data: © OpenStreetMap contributors. c) Climate trend of the AEMET station Almeria (6297), closest to our Aguamarga station, and precipitation during hydrological years 2022/2023 and 2023/2024 of the same station. The period of the SCARCE campaign is highlighted. (For interpretation of the references to colour in this figure legend, the reader is referred to the web version of this article.)

et al., 2010; Petters et al., 2024; Rasheeda Satheesh et al., 2024), where the power spectral density for daytime data followed the −5/3 power law in the intermediate frequencies. For this time interval, the total variance of β_{att} (given by the integral of its spectrum) decreased with height, indicating that the aerosol particles approached well-mixed conditions.

On the other hand, the non-convective density functions (Fig. 3c and d) did not follow −5/3 power law. However, the available literature either focused on daytime period or did not show examples for nighttime data, so a comparison for our non-convective spectra is not possible. Nevertheless, the flattening of the slope during nighttime indicates lack of convection and stratification as expected during nighttime periods. Karasewicz et al. (2024) confirmed with Doppler lidar data that during the convective regime, Kolmogorov's hypothesis is fulfilled for the inertial subrange, while non-convective regimes deviate from the classic theory of turbulence and other turbulence theories apply (e.g., Obligado and Vassilicos, 2019). This deviation of the classical equilibrium theory and the similarity with non-equilibrium theories is observed specially for w in Fig. 3d, while analysis of β_{att} spectrum during nighttime suggested stable conditions.

The stationarity test described in Sect. 3.2 was applied to the entire dataset from the campaigns. Of the original 260,406 values available, 55 % were classified as valid after the stationarity test, resulting in 144,176 values used for further analysis. The filtering was consistent across both daytime and nighttime intervals. Notably, 97.5 % of the values from the lowest observational level passed the test, indicating that this level was minimally affected by non-stationarity.

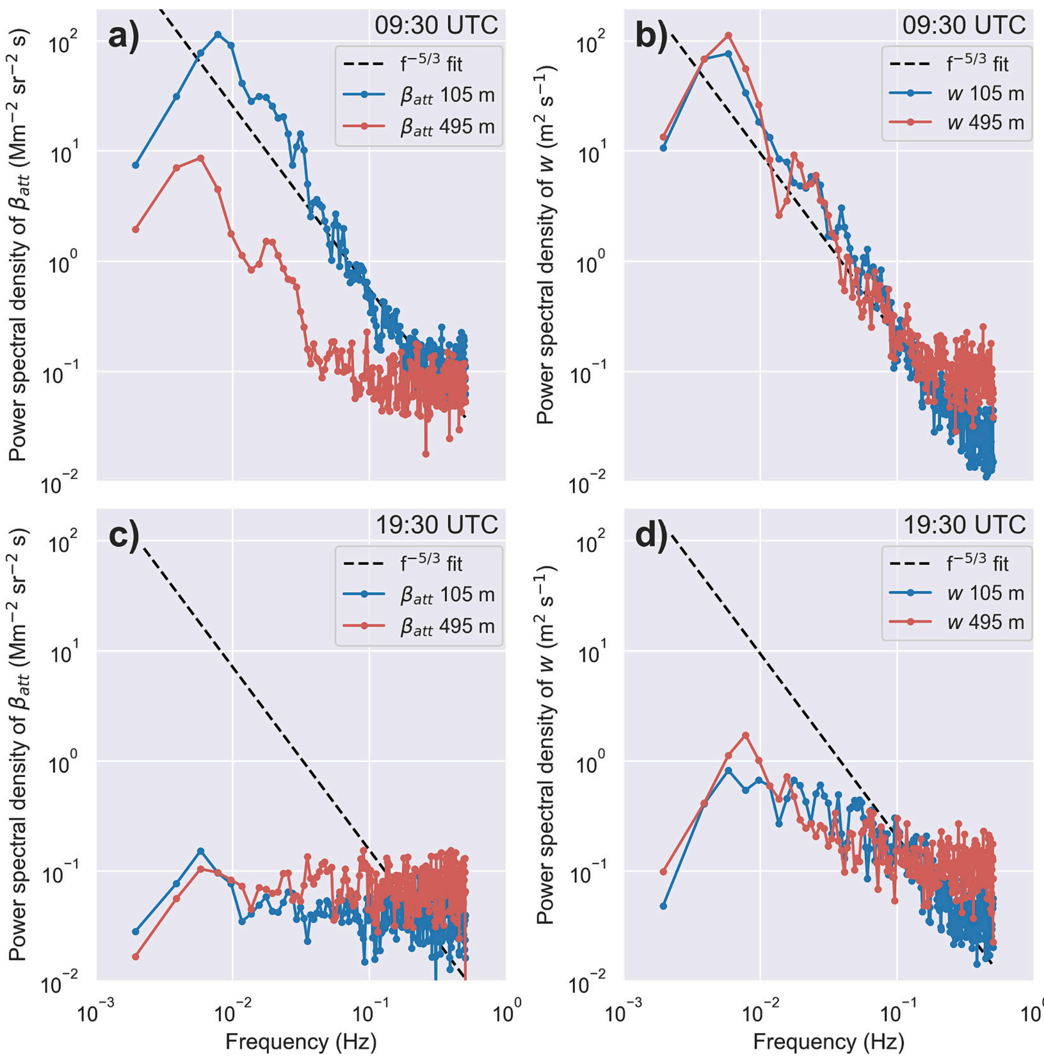

Fig. 3. Power spectral density of β_{att} (in Mm^{-2} sr^{-2} s) and w (in m^2 s^{-1}) for the period from 09:30 to 10:30 UTC (convective) and from 19:30 to 20:30 UTC (non-convective) on 10 April 2023 (BLOOM II) at 105 and 495 m with a time resolution of 1 s. Black dashed line indicates the expected −5/3 slope in the inertial subrange, fitted for the 105 m function but comparable to the 495 m function.

4.3. Characterizing a clear-sky convective-ruled day

According to ceilometer data (Fig. 4a), 25 April 2023 (BLOOM II) was a clear day with negligible cirrus presence (up to 10 km) during daytime. Some cirrus clouds were detected around 04:00 UTC, not affecting the convective regimes. The AERONET sun-photometer provided a mean AOD$_{500}$ of 0.13 ± 0.02, indicating a fairly clean atmosphere given the location of the station, with a mean AE$_{440–870}$ of 1.03 ± 0.17 and FMF$_{500}$ of 0.53 ± 0.06. Due to the low aerosol load, no valid AERONET inversion product was available. The NAAPS and BSC-DREAM8b models did not forecast the presence of transported dust or smoke over the regions (not shown).

According to the Doppler lidar turbulence source classification (Fig. 4b), convection dominated from 8 to 19 UTC (daytime), while wind shear was responsible for the turbulence before 6 UTC and after 20 UTC (nighttime). The ε estimated by the Doppler lidar (Fig. 4c) showed a clear difference between daytime and nocturnal behavior, with lower values before 8 UTC and after 19 UTC, and larger values from 8 to 19 UTC in the whole vertical column. Significant values were observed at the highest altitudes detected by the Doppler lidar.

Fig. 4d illustrates the v_t pattern for a clear-sky convective-ruled day. When convection started, at 8 UTC, turbulence increased and consequently v_t increased and became positive, indicating upward transport of particles. Additionally, positive values of v_t seemed to spread upwards, attaining maximum altitude around noon, which is related to the development of the boundary layer (Nilsson et al., 2001). Thus, atmospheric instability, with ε values greater than 10^{-4} m^2 s^{-3}, promoted upward transport, reaching a maximum v_t of 14 cm s^{-1}. During night, atmospheric stability inhibited significant transport in any direction. A similar diurnal pattern was reported by Petters et al. (2024) and by Rasheeda Satheesh et al. (2024). An average v_t of (1.6 ± 3.0) cm s^{-1} was observed for the whole day, while (3.0 ± 3.7) cm s^{-1} was observed during the convective regime (from 8 to 19 UTC) and an almost null upward/downward transport of (0.01 ± 0.54) cm s^{-1} during the rest of the period. Thus, these v_t indicated that upward transport of particles was taking place over the station, suggesting that our landscape behaves as a net source of particles under this specific atmospheric condition.

A similar case (dry, cloud-free convective boundary layer) was analyzed by Engelmann et al. (2008). They ultimately retrieved particle mass flux profiles ($\overline{m'w'}$, in μg m^{-2} s^{-1}) from backscatter coefficient flux profiles ($\overline{\beta'w'}$, in Mm^{-1} sr^{-1} m s^{-1}) and a “temporally and vertically constant” conversion factor ($\overline{m}/\overline{\beta}$ of around 21.1 μg m^{-3} Mm sr). In the mentioned study, Fig. 2 shows an approximate $\overline{\beta}$ value of 1.9 Mm^{-1} sr^{-1} at around 1 km between 12 and 14 UTC, which would yield a $\overline{m}$ value of 40.1 μg m^{-3} taking into account the conversion factor, while Fig. 10 shows an approximate $\overline{m'w'}$ value of 2.8 μg m^{-2} s^{-1} at the same height

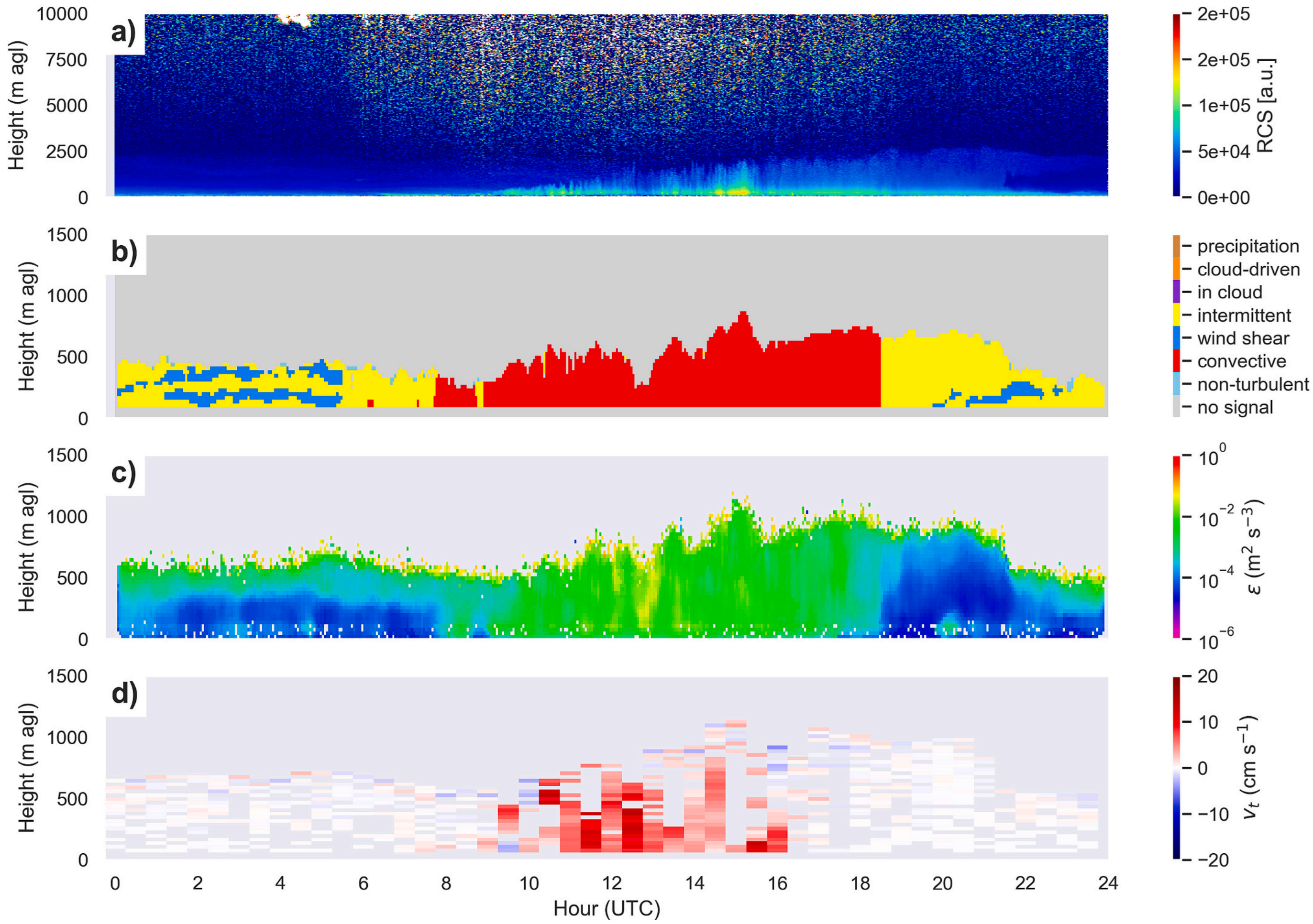

Fig. 4. Time series of the vertically resolved a) RCS (in arbitrary units) at 1064 nm observed by the ceilometer, b) turbulence source classification within the ABL and c) ε (in m^2 s^{-3}) provided by the Doppler lidar, and d) quality checked v_t (in cm s^{-1}) retrieved by the Doppler lidar, over Guadiana-UGR on 25 April 2023.

and time. Applying the normalization to obtain v_t, dividing the particle mass concentration fluxes by the obtained particle mass concentration, one can obtain a maximum v_t of around 7 cm s^{-1}. This value measured in Leipzig, Germany, is of the same order of magnitude as those presented in this case study (Fig. 4d), although it is significantly lower than the maximum v_t recorded on 25 April 2023 (BLOOM II).

An analogous comparison was carried out with the results obtained by Wang et al. (2021). A maximum vertical aerosol mass flux of around 2.5 μg m^{-2} s^{-1} was obtained (from their Fig. 6, not to be confused with the integrated values presented in their Fig. 7), for an aerosol mass concentration of 27.4 μg m^{-3}, which yields a v_t of around 9 cm s^{-1} applying the aforementioned normalization. This result is in agreement with the orders of magnitude of the v_t obtained here (Fig. 4d).

4.4. Cloud and horizontal wind effects on particle transport

The previously observed pattern for a cloud free day during which convection dominated daytime turbulence could be understood as an ideal case rarely observed. The 6 April 2023 was a cloud-covered day as observed in Fig. 5a. This cover seemed to restrain convection, suppressing development of the boundary layer. In fact, Fig. 5b showed that the convective mixing classification reached significantly lower altitude than that observed in Fig. 4b. Slightly lower values were observed during the convective period (Fig. 5c), probably due to suppression of convection by cloud cover. However, ε values larger than 10^{-4} m^2 s^{-3} were observed after 19 UTC associated with significant horizontal winds (Fig. 5d) close to the surface activating the eddies and, consequently, activating ε (mechanical turbulence). A significant increase in aerosol load was observed after 19 UTC in the lowermost atmospheric region (Fig. 5a). Due to the significant and complete cloud cover, no AERONET data were available for this day.

The v_t time series can be observed in Fig. 5e. Significant upward transport of particles were observed after 8 UTC. However, in this case, v_t was significantly lower, associated with the weaker convective activity within the boundary layer due to the cloud cover. An average v_t of (0.7 ± 1.4) cm s^{-1} was recorded for the whole day. An average v_t of (0.9 ± 1.3) cm s^{-1} was observed during the convective regime (from 8 to 19 UTC), while an average v_t of (0.6 ± 1.5) cm s^{-1} was recorded for the rest of the period. The specific period between 19 and 21 UTC exhibited an average v_t of (2.0 ± 2.5) cm s^{-1}, a significant non-convection-associated upward transport. From these values, one could conclude that for this cloudy day, with lower convective activity, upward transport was reduced with respect to the cloud-free day with higher convective activity (e.g., Lamaud et al., 1994; Vong et al., 2004; Pryor et al., 2008). Additionally, it was observed that high horizontal winds close to the surface could significantly impact vertical transport. These high horizontal winds were recorded as high turbulent activity in the ε values (Fig. 5c), with values greater than 10^{-4} m^2 s^{-3}. Previous studies have pointed to higher exchanges during high horizontal wind conditions (e.g. Sievering, 1987; Pryor et al., 2008), while a comparable injection of particles in the boundary layer was observed by Rasheeda Satheesh et al. (2024).

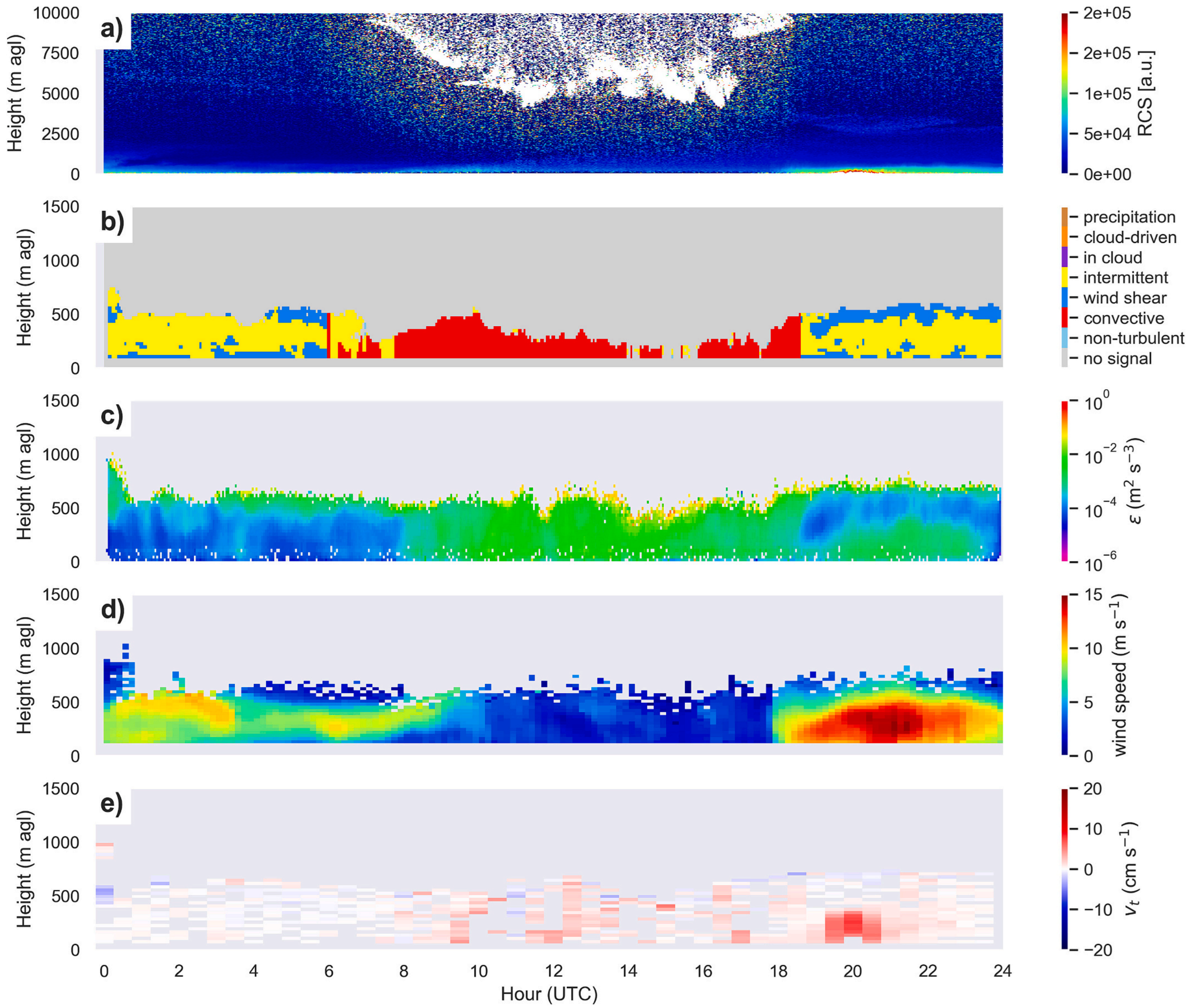

Fig. 5. Time series of the vertically resolved a) RCS (in arbitrary units) at 1064 nm observed by the ceilometer, b) turbulence source classification within the ABL, c) ε (in m^2 s^{-3}) and d) horizontal wind speed (in m s^{-1}) provided by the Doppler lidar and e) quality checked v_t (in cm s^{-1}) retrieved by the Doppler lidar, over Guadiana-UGR on 6 April 2023, a cloudy day.

4.5. Downward transport during dust outbreaks

Saharan dust outbreaks occur frequently over Southern Spain (Cazorla et al., 2017; López-Cayuela et al., 2021; Salgueiro et al., 2021). On 17 June 2022 a significant dust layer was located over the station of Guadiana-UGR, as observed in Fig. 6a. Ceilometer data indicated the presence of a significant dust layer up to 3 km and lesser amounts up to 5 km. The AERONET data showed a mean AOD_{500} of 0.37 ± 0.01, a mean $AE_{440–870}$ of 0.13 ± 0.01 and a mean FMF_{500} of 0.18 ± 0.01. These values indicate the presence of a significant load of coarse particles. AERONET inversion products confirmed the majority of coarse particles in volume, while the presence of dust particles was supported by both the NAAPS and BSC-DREAM8b models, from 11 to 21 June 2022 (not shown). A thick cloud is also detected between 8 and 12 UTC. According to the turbulence source classification provided by the Doppler lidar (Fig. 6b) convection dominated from 8 to 20 UTC, while non-turbulent regimes were found between 4 and 7 UTC. The same was observed in the ε values (Fig. 6c), with values greater than 10^{-4} m^2 s^{-3} mainly between 8 and 16 UTC, similar to those observed for the case with cloud cover. Clear stratification was indicated between 4 and 7 UTC, with ε values lower than 10^{-4} m^2 s^{-3}.

The v_t obtained can be observed in Fig. 6d. The periods between 1 and 3 UTC and between 19 and 22 UTC were characterized by small but yet significant negative v_t, indicating downward transport of particles. The behavior observed between 8 and 18 UTC was similar to that observed for the cloudy case, except for the period between 10 and 13 UTC. Convection seemed to influence vertical transport during this period but due to the cloud cover the observed values are smaller than those observed during a cloud-free day, and between 10 and 13 UTC downward transport of particles was observed. An average v_t of (0.2 ± 1.3) cm s^{-1} was recorded for the whole day, while (0.5 ± 1.5) cm s^{-1} was observed from 8 to 20 UTC (convective regime) and (−0.1 ± 0.6) cm s^{-1} during the rest of the period (non-convective). The average v_t for the whole day was lower than those observed for the cloud-free day and the cloudy day, and so was the observed averaged v_t during the convective regime. Additionally, the v_t observed during the non-convective period was one order of magnitude larger (in absolute value) than that observed for the cloud-free day, indicating that

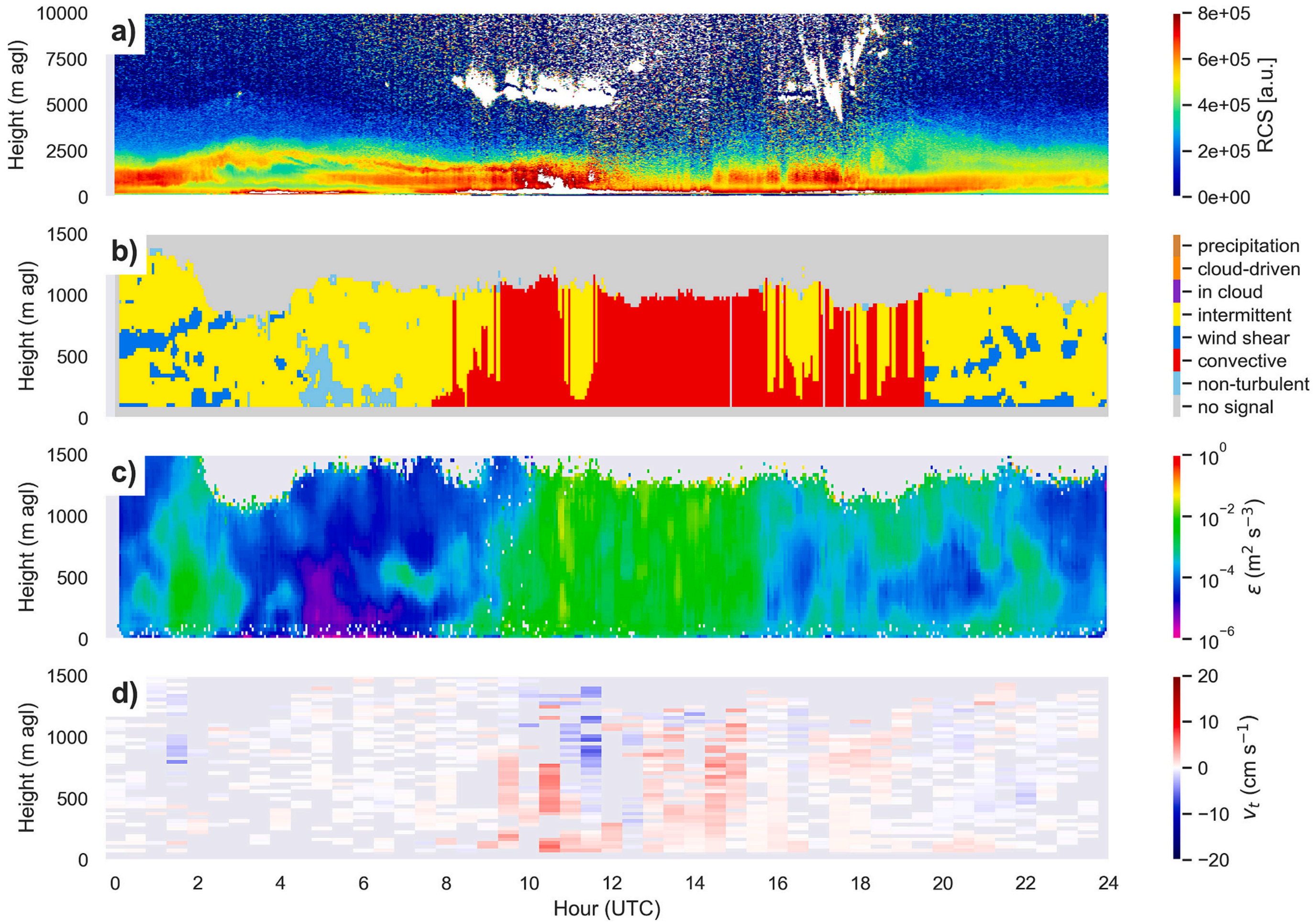

Fig. 6. Time series of the vertically resolved a) RCS (in arbitrary units) at 1064 nm observed by the ceilometer, b) turbulence source classification within the ABL and c) ε (in m^2 s^{-3}) provided by the Doppler lidar, and d) quality checked v_t (in cm s^{-1}) retrieved by the Doppler lidar, over Guadiana-UGR on 17 June 2022.

downward transport of particles was more significant at night with significant dust presence. Out of all of the v_t values recorded, 43 % were negative, versus 37 % in the case of the clear convection-dominated day. Thus, downward transport regimes were more frequent during this Saharan dust outbreak. This deposition was enhanced by a positive dust gradient, as coarse particles exhibit larger surface impaction efficiency, and greater stop distances (Fuchs, 1964). This created an upward positive gradient, leading to a downward flux. Similar findings were reported by Bergametti et al. (2018), who observed larger downward transport (deposition) of particles during dust events in a semi-arid landscape.

4.6. Campaign comparison

4.6.1. Flux footprint analysis

In order to estimate the representativeness of the fluxes captured, a flux footprint analysis was carried out, with special focus on the measurement height (z_m) of 105 m, the lowermost observational level of the Doppler lidar which ranges from 90 to 120 m. The distance from the instrument to the maximum footprint contribution (x_{max}) was calculated for each campaign in 30-min intervals and subsequently plotted onto satellite images (Fig. 7) of the station regions, taking into account the wind direction for each specific 30-min interval. Two distinct scenarios were considered based on the turbulence source classification (convective and non-convective).

Fig. 7a and b display the x_{max} locations for the lowest observational level and for each 30-min interval of BLOOM and BLOOM II. Fig. 7a corresponds to the convective intervals, associated with daytime convection, which appeared to be less scattered and generally closer to the station, with median values (considering 15° angular intervals) within 500 m from the instrument. Additionally, most of the convective x_{max} were found within 1000 m from the instrument (95 % of all values). On the other hand, Fig. 7b corresponds to the non-convective intervals, associated with nighttime regimes, whose median values are found between 500 and 1000 m around the instrument. Although most non-convective values were also found within 2000 m from the instrument (92 %), these values were more scattered than the convective ones, and some values extended to greater distances, reaching up to 2500 and even 3000 m, associated with nighttime conditions and low turbulence. As expected, the non-convective cases exhibited the x_{max} at a greater distance (Cooper et al., 2003). Both scenarios exhibit two main modes according to the direction of x_{max}, which correspond to the two modes observed in the wind roses (Fig. 1b). Since the region features homogeneous land use for several kilometers in all directions, the turbulent fluxes captured at the lowest Doppler lidar observational level were well within the fetch and could reliably be associated with the studied ecosystem.

A similar behavior was observed for the 30-min x_{max} calculations during SCARCE (Fig. 7c and d) for the lowest observational level. Convective x_{max} values (Fig. 7c) were mostly constrained within 1000 m around the instrument (98 % of all values), with the median values found within 500 m. A similar pattern was observed for the non-convective x_{max} values (Fig. 7d), although some extended to greater distances, up to 2500 m. Two main modes were evident, corresponding

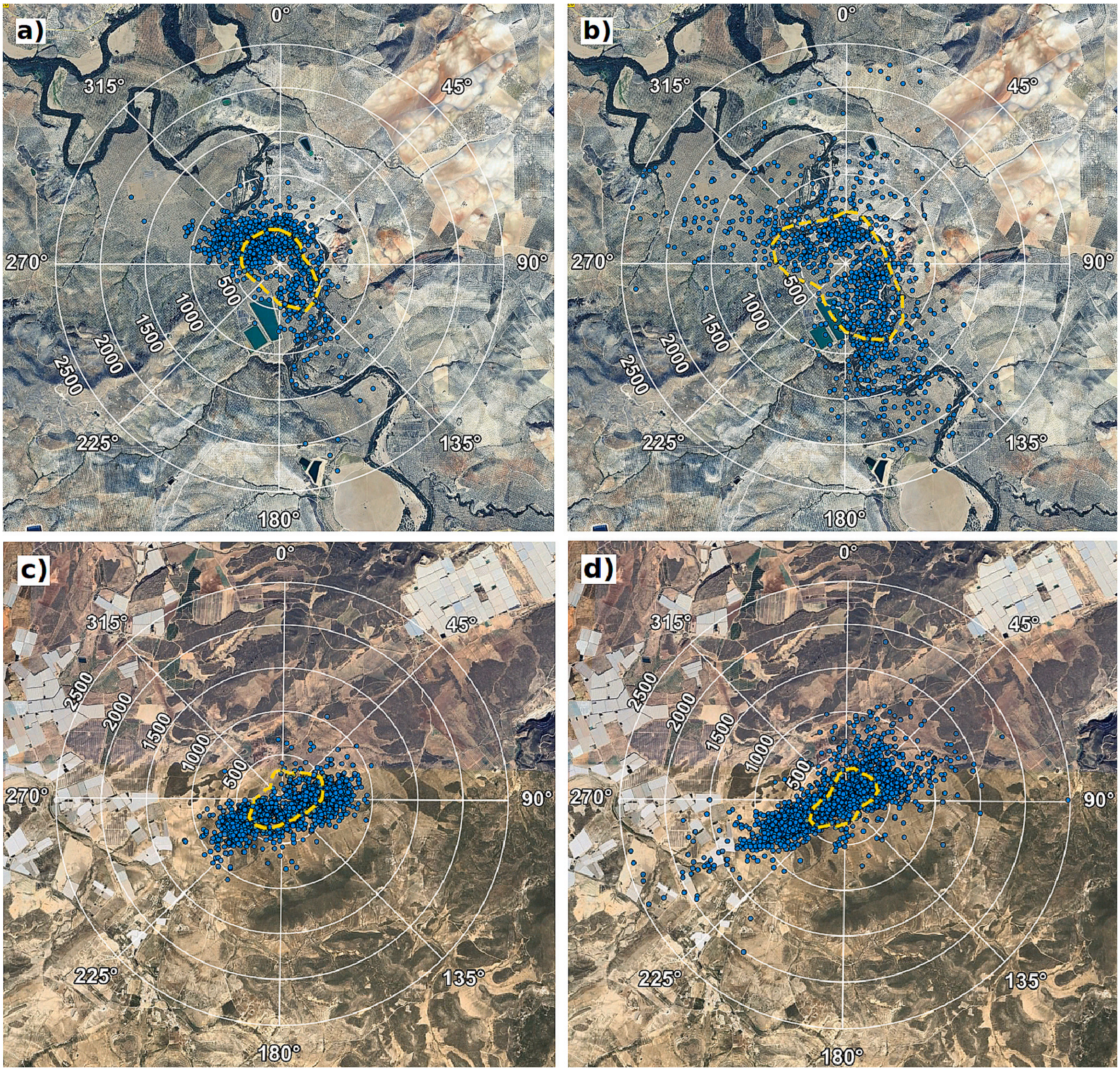

Fig. 7. Satellite images of the stations: (a) and (b) correspond to Guadiana-UGR, while (c) and (d) correspond to Aguamarga. The radial axis represents distance (m) from the instrument, and the angular axis indicates direction based on wind direction. The meteorological convention is used for the wind direction, i.e., direction indicates the origin of the wind. Blue dots mark each 30-min calculation of x_{max}, while the yellow dashed line represents the median x_{max} values computed within 15° intervals. (a) and (c) correspond to the convective scenarios, while (b) and (d) correspond to the non-convective (including non-turbulent, wind shear and intermittent) according to the Doppler lidar turbulence source classification scheme. Satellite image: Landsat/Copernicus. (For interpretation of the references to colour in this figure legend, the reader is referred to the web version of this article.)

to the wind direction modes (Fig. 2b). Given that the region is relatively homogeneous in all directions for a few kilometers – encompassing the median values and most of the x_{mas} locations – the turbulent fluxes captured at the lowest observational level remained within the Cabo de Gata Natural Park and could be reliably associated with the studied ecosystem.

Footprint calculations were conducted across the entire vertical range of the Doppler lidar profiles, revealing that the location of the maximum footprint contribution shifts further upwind with increasing altitude within the boundary layer. A similar analysis was performed for the observational level of 495 m. At Guadiana-UGR, the median convective x_{max} values were located around 2.5 km, with most values constrained within 5 km (82 % of all values) and some extending up to 10 km. Non-convective median values increased to around 10 km, with most values found within 20 km (83 %). In contrast, at Aguamarga, both convective and non-convective median values remained at around 2.5 km, with most values confined within 7.5 km (80 %) and some reaching up to 10 km.

At Guadiana-UGR, the region is sufficiently homogeneous over several kilometers, and most turbulent fluxes captured at 495 m can be associated with the same ecosystem type (olive grove), albeit at a broader landscape scale. However, the landscape around Aguamarga is more heterogeneous, with numerous greenhouses located to the west. As a result, the turbulent fluxes captured at 495 m at Aguamarga may be influenced by these inhomogeneities, integrating contributions from various surface types, although the exact impact of greenhouses is unknown. Therefore, the higher the flux measurement height, the further upwind their source shifts (Wang et al., 2006; Eichinger and Cooper, 2007), reducing its representativeness for the specific ecosystem where the instrument is located, though the measurements remain representative at the landscape level.

The flux footprint analyses revealed that the particle fluxes captured by the Doppler lidar between 90 and 120 m were representative of the studied ecosystems as these ecosystems are homogeneous within the maximum footprint contribution location and the instrument. In fact, this sampling altitude is not far from the altitude of eddy towers and tall towers. Therefore, the name of *emission* velocity might be adequate for the calculated vertical transport velocities at this specific vertical range, as actual emissions from the surface were being captured. Thus, Doppler lidars are capable of measuring ecosystem-scale coarse particle emission and deposition, as eddy towers do. Furthermore, the maximum footprint contribution location shifts further away from the instrument for higher measurement. As these ecosystems are relatively homogeneous for kilometers around, the Doppler lidars were proven to be capable of measuring landscape-scale particle vertical transports, unlike most eddy towers.

4.6.2. Transport velocity in the vertical range

Specific case studies helped to visualize the main atmospheric phenomena affecting particle transport. However, averaging for longer periods could yield typical trends, improving the statistical significance of the lidar flux profiles (Senff et al., 1994). According to the periods stated in Section 4.1, the average v_t values, temporally and vertically resolved, for each campaign are presented in Fig. 8, yielding the average patterns exhibited by the v_t during BLOOM (Fig. 8a), BLOOM II (Fig. 8b) and SCARCE (Fig. 8c). Only averages with 20 % of valid data were considered as acceptable.

Analogous behavior was observed for the three campaigns (Table 1, rows a, b, c), with similar mean v_t values. For the three campaigns positive v_t were more abundant, with almost 2 out of 3 values being between -1 and 1 cm s^{-1}, and very few with downward transport of magnitude exceeding 1 cm s^{-1}. The median values for the three campaigns were positive, corroborating a net upward transport of particles.

A significant increase in v_t was observed to start between 6 and 8 UTC (Fig. 8), when convective mixing and boundary layer development generally started (Nilsson et al., 2001). Positive v_t values developed vertically with time, reaching the maximum height at around 12 UTC. The maximum height was related to the boundary layer development, varying from around 0.8 km for SCARCE and BLOOM II to 1.15 km for BLOOM. After 14 UTC, positive v_t values were observed to reduce both in value and in height. BLOOM's maximum height was significantly larger than that observed for BLOOM II,. This difference may be

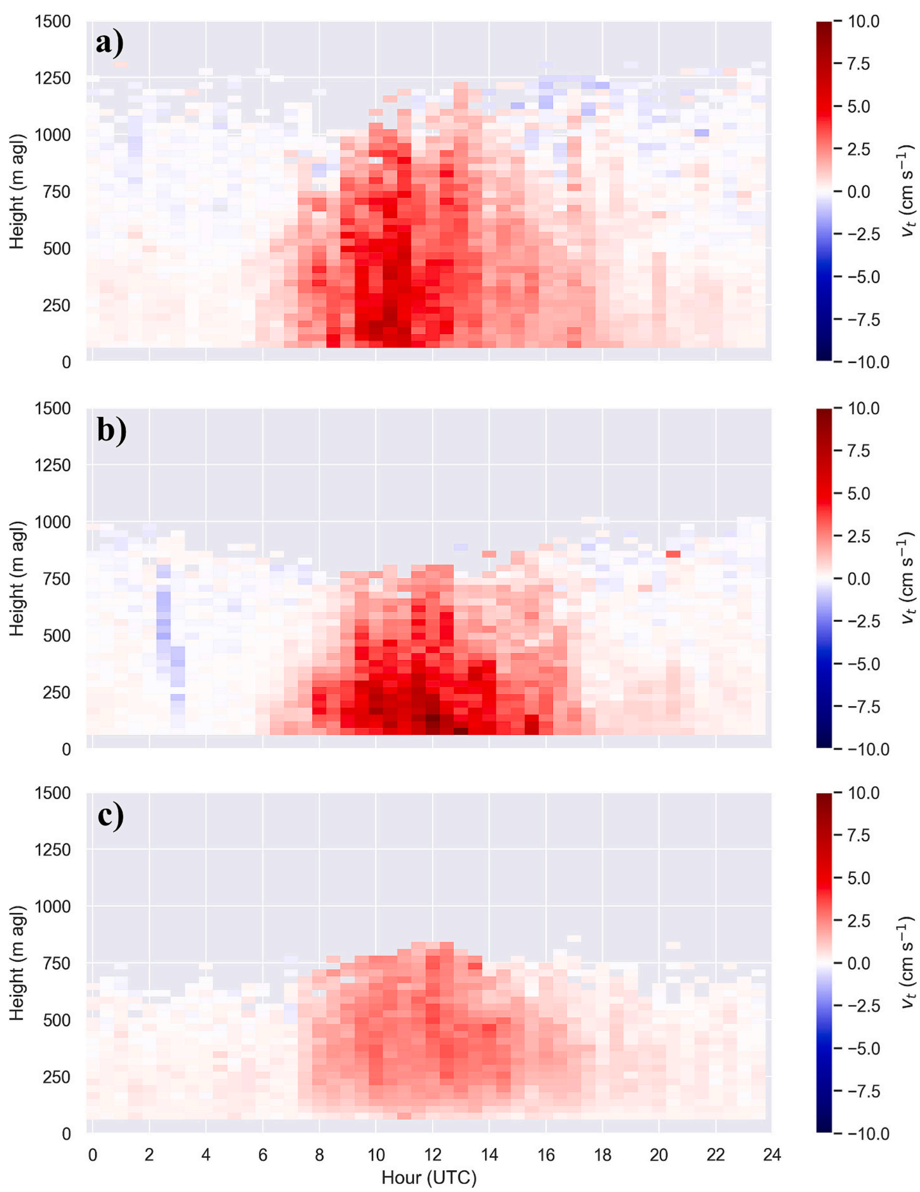

Fig. 8. Time series of the vertically resolved v_t averages for a) BLOOM, b) BLOOM II and c) SCARCE.

Table 1
Statistical analysis of the v_t at all heights for each campaign (BLOOM, BLOOM II and SCARCE) and the daytime (d) and nighttime (n) periods, featuring the number of counts, mean, standard deviation (SD), median, percentage of positive values, percentage of values between -1 cm s^{-1} and $+$ 1 cm s^{-1} and percentages of values greater than $+1$ cm s^{-1} and lesser than -1 cm s^{-1}.

	campaign	counts	mean cm s^{-1}	SD cm s^{-1}	median cm s^{-1}	% of positive v_t	% of $\lvert v_t\rvert < 1$ cm s^{-1}	% of $v_t > +1$ cm s^{-1}	% of $v_t < -1$ cm s^{-1}
(a)	BLOOM	29,307	1.10	2.83	0.31	66	63	31	6
(b)	BLOOM II	36,914	1.12	3.89	0.24	62	63	30	7
(c)	SCARCE	77,955	0.90	2.83	0.20	62	66	26	8
(d)	BLOOM d	14,463	2.10	3.67	1.20	77	37	54	9
(e)	BLOOM II d	15,066	2.62	5.53	1.48	78	31	59	10
(f)	SCARCE d	40,789	1.56	3.55	0.61	67	48	42	11
(h)	BLOOM n	14,844	0.13	0.87	0.08	56	89	8	3
(i)	BLOOM II n	21,848	0.09	1.37	0.02	51	85	9	6
(j)	SCARCE n	37,166	0.18	1.40	0.07	57	86	9	5

seasonal, with BLOOM extending into June, a month with generally higher boundary layer development than that for BLOOM II, which ended in May. Nevertheless, BLOOM II exhibited larger v_t closer to the surface, possibly due to dryer soil conditions (Donateo et al., 2023). However, the differences in the meteorological conditions are an important driver (Fernandes et al., 2023). Different behavior was observed for SCARCE, with lower v_t closer to the surface than above, from 7 to 18 UTC. This decoupling from the surface might be related to weaker convection taking place over the coastal station of Aguamarga. Thus, during daytime, convective mixing seems to be the main driver of upward transport of particles, especially inland (Guadiana-UGR). Compared to the average of the whole campaign (Table 1, rows a, b and c), daytime (convective regime) exhibited a significant increase in both the mean and median v_t (Table 1, rows d, e and f), while the positive v_t values, as well as those with $|v_t|$ greater than 1 cm s^{-1} became more frequent. Thus, neutral values with $|v_t|$ lower than 1 cm s^{-1} became less frequent.

Before 6 UTC and after 18 UTC, v_t was significantly lower at both stations (Fig. 8 and Table 1, rows g, h and i), coinciding with periods of no convective mixing and shear-induced turbulence. This reduction in v_t was more pronounced at the inland station, sometimes even displaying average negative values, while the coastal station shows lower but more significant and positive v_t values during these hours. An area of positive v_t is observed close to the surface in BLOOM and BLOOM II average patterns between 18 and 22 UTC, with slightly larger v_t values indicating that the high horizontal wind observed in Sect. 4.4 might be a frequent phenomenon at the station. Mean and median v_t indicated net upward transport also at night. Additionally, around half of the v_t were positive, indicating that negative values are almost as frequent as positive ones. Furthermore, almost 90 % of them had $|v_t|$ lower than 1 cm s^{-1}, corroborating that this period had lower transport magnitudes.

Doppler lidar measurements produce numerous products owing to the temporal and vertical resolution of the measurements. Recognizing this, it became imperative to target specific regions for detailed analysis. The study shifts its focus to the lowermost observational level, ranging from 90 to 120 m, as it offers the most representative measurements for studying landscape fluxes.

4.6.3. Transport velocity at the lowermost observational level

Table 2 focuses on v_t for the lowest Doppler vertical observational level and gathers statistical analyses analogous to those presented in Table 1. In this range, the patterns of each campaign are significantly different. Mean and median v_t (Table 2, rows a, b and c) suggest that both Guadiana-UGR and Aguamarga were net sources of particles. However, BLOOM II displayed a significantly larger mean value than BLOOM, possibly due to its drier soil conditions. Petters et al. (2024), with a comparable methodology in a humid climate regime, observed a similar consistent positive emission regime. SCARCE exhibited significantly lower mean and median values, indicating that emission from the coastal station was less significant than inland. In fact, the percentage of $|v_t|$ less than 1 cm s^{-1} was significantly larger during SCARCE, indicating more neutral behavior.

During daytime (Table 2, rows d, e and f) again BLOOM II exhibited a significantly larger average v_t than BLOOM, while the SCARCE average v_t remained low but positive. The situations with v_t larger than $+1$ cm s^{-1} were the most frequent at the inland station, where around 85 % of v_t values were positive. SCARCE showed a different pattern, with $|v_t|$ less than 1 cm s^{-1} significantly more frequently. However, emission regimes dominated at both stations. The turbulence source classification indicates that daytime turbulence is mostly dominated by convection, with the major source from 7 to 19 UTC inland and from 8 to 17:30 in the coastal station.

During nighttime (Table 2, rows g, h and i), the three campaigns exhibited very similar patterns with lower but positive mean and median v_t. In this regime, most of the v_t laid between -1 cm s^{-1} and $+$ 1 cm s^{-1}. In all cases, emission dominated deposition, indicating that even at night the stations act as net sources of particles, similarly to what Petters et al. (2024) observed. Wind shear is the primary source of nighttime turbulence in the inland station, while it is almost negligible in the nighttime of the coastal station.

While this study has conducted a comparative analysis of different campaigns, it becomes crucial to acknowledge the influence of factors like atmospheric variability and soil conditions. Previous research has highlighted the significance of these variations when assessing particle fluxes over consecutive years in dryland ecosystems (Fernandes et al.,

Table 2
Statistical analysis of the v_t captured in the lowermost range, from 90 to 120 m, for each campaign (BLOOM, BLOOM II and SCARCE) and the daytime (d) and nighttime (n) periods, featuring the number of counts, mean, standard deviation (SD), median, percentage of positive values, percentage of values between -1 cm s^{-1} and $+$ 1 cm s^{-1} and percentages of values greater than $+1$ cm s^{-1} and lesser than -1 cm s^{-1}.

	campaign	counts	mean cm s^{-1}	SD cm s^{-1}	median cm s^{-1}	% of positive v_t	% of $\lvert v_t\rvert < 1$ cm s^{-1}	% of $v_t > +1$ cm s^{-1}	% of $v_t < -1$ cm s^{-1}
(a)	BLOOM	1604	1.27	2.90	0.39	77	63	34	3
(b)	BLOOM II	2517	1.79	5.42	0.29	71	62	34	4
(c)	SCARCE	6506	0.58	2.06	0.16	65	69	23	8
(d)	BLOOM d	766	2.37	3.83	1.40	86	33	61	6
(e)	BLOOM II d	1091	3.81	7.64	1.97	86	25	68	7
(f)	SCARCE d	3133	1.00	2.68	0.57	67	48	39	13
(h)	BLOOM n	838	0.27	0.73	0.12	69	91	8	1
(i)	BLOOM II n	1426	0.24	1.28	0.07	59	90	8	2
(j)	SCARCE n	3373	0.19	1.09	0.08	64	90	8	2

2023). In fact, the dynamics within the boundary layer and the atmospheric boundary layer development are primary mechanisms affecting particle concentrations and exchanges (Nilsson et al., 2001; Rannik et al., 2009) and they can exhibit a significant variability.

5. Conclusions

A methodology to retrieve particle transport from stand-alone Doppler lidar measurements was presented in this study. The methodology was applied to three different campaigns in Southeastern Spain, namely BLOOM and BLOOM II in Guadiana-UGR (an extensive traditional olive grove) and SCARCE in Aguamarga (a rural station in Cabo de Gata-Níjar Natural Park near the coast), with the aim of identifying the daily patterns and the drivers for particle transport over Mediterranean drylands. Initially, fluxes of quasi-particle backscatter coefficients were obtained, using the software provided by Ortiz-Amezcua (2023), which were ultimately normalized by the backscatter coefficients in order to retrieve profiles of the vertical transport velocity, v_t.

The generated database allowed us to test the methodology under various atmospheric conditions, and the effects of several atmospheric phenomena were presented in case studies. Convective mixing and boundary-layer development were found to be the primary drivers of net upward particle transport. However, this effect was influenced by other atmospheric conditions. Clouds suppressed convection, encouraging atmospheric stability and preventing vertical transport, while significant horizontal winds were found to increase mechanically-driven turbulence and, consequently, upward transport. During a notable Saharan dust outbreak, substantial downward transport of particles was observed.

Each campaign was analyzed as a whole, filtering precipitation situations for the sake of data quality, so that dry particle transport was assessed. A general net upward transport of particles was found across the atmospheric boundary layer during convective regimes, and even at night, especially during SCARCE. However, significantly lower vertical transport was found during non-convective periods for all campaigns. Upward transport of particles was larger at Guadiana-UGR during the convective period, reaching higher altitudes due to the higher boundary layer development of the inland station, compared to the maritime boundary layer of the coastal station.

Analysis of the flux footprint at the lowermost observational level of the retrieved v_t profiles, between 90 and 120 m, suggested that most of the measured transport was associated with exchanges within the studied dryland ecosystems. Given the homogeneity of the ecosystem in such footprints the potential of the Doppler lidar to measure ecosystem-scale turbulent fluxes (emission and deposition) was evidenced, similarly to most eddy towers. Additionally, footprint analyses at higher Doppler lidar observational levels revealed that higher sampling altitudes enlarge the flux footprint beyond the ecosystem scale. Therefore, the potential of the Doppler lidar to measure landscape-scale turbulent fluxes (upward and downward transport) within the boundary layer was also proven, highlighting a significant advantage of remote sensing techniques over conventional in-situ methods.

Clear and consistent average particle emission was found at the lowermost observational level during the three campaigns, confirming that these drylands were net sources of particles during the studied periods. Emission at the inland station of Guadiana-UGR was found to be significantly larger than at the coastal station of Aguamarga, especially during convective regimes. Ultimately, a possible effect of soil aridity was observed between BLOOM and BLOOM II, the second campaign taking place during a period of more arid soil and no vegetation cover, and exhibiting slightly larger emissions near the surface. Finally, particle transport was observed to depend largely on atmospheric phenomena like convective mixing and wind shear.

The patterns of particle transport over two different Mediterranean dryland ecosystems were analyzed with a novel methodology for Doppler lidars, revealing the main atmospheric mechanisms impacting the exchanges. These findings provide new insights into coarse particle exchanges in drylands environments. These ecosystems are expanding as a result of climate change and are recognized as key mineral dust sources. The results contribute to the currently limited understanding of the turbulent particle exchanges over semiarid landscaped and confirm their role in dust emissions, with important implications for air quality and climate modeling. Furthermore, the implications of this methodology seem promising, as a stand-alone configuration for the Doppler lidar can be easily implemented in basic processing chains of the Doppler lidar system. However, we have seen that their representativity and interpretation is not straightforward and should be carefully addressed in future applications.

CRediT authorship contribution statement

Jesús Abril-Gago: Writing – review & editing, Writing – original draft, Methodology, Investigation, Formal analysis, Data curation, Conceptualization. **Pablo Ortiz-Amezcua:** Writing – review & editing, Methodology, Investigation, Formal analysis, Data curation, Conceptualization. **Andrew S. Kowalski:** Writing – review & editing, Writing – original draft, Methodology, Investigation, Formal analysis, Data curation, Conceptualization. **Juan Antonio Bravo-Aranda:** Writing – review & editing. **María José Granados-Muñoz:** Writing – review & editing. **Juana Andújar-Maqueda:** Writing – review & editing, Formal analysis, Data curation. **Lucas Alados-Arboledas:** Writing – review & editing, Resources, Funding acquisition. **Juan Luis Guerrero-Rascado:** Writing – review & editing, Writing – original draft, Resources, Project administration, Methodology, Investigation, Funding acquisition, Formal analysis, Data curation, Conceptualization.

Code availability

The code for processing Doppler lidar measurements into fluxes is provided by Ortiz-Amezcua (2023).

Declaration of competing interest

The authors declare that they have no known competing financial interests or personal relationships that could have appeared to influence the work reported in this paper.

Acknowledgments

This work was supported by the project INTEGRATYON[3] (PID2020-117825GB-C21 and PID2020-117825GB-C22) funded by MICIU/AEI/10.13039/501100011033, and by University of Granada Plan Propio through Excellence Research Unit Earth Science and Singular Laboratory AGORA (LS2022-1) program, by the European Union's Horizon 2020 research and innovation program through project ACTRIS.IMP (grant agreement No 871115) and the strategic network ACTRIS-España (RED2022-134824-E), by Junta de Andalucía through project MORADO (C-366-UGR23), and by University of Granada Plan Propio programs Visiting Scholars (PPVS2024-06), Excellence Research Unit Earth Science and Singular Laboratory AGORA (LS2022-1) and Project for Early-Career Researchers EMITE-EC (PPJIB-2024-12). This study is part of a project that is supported by the European Commission under the Horizon 2020 – Research and Innovation Framework Programme, H2020-INFRAIA-2020-1, Grant Agreement number: 101008004. Jesús Abril-Gago received funding through the grants FPU21/01436 and EST24/00285 funded by MICIU/AEI/10.13039/501100011033. Funding for open access charge: Universidad de Granada/CBUA.

Data availability

The Doppler lidar and ceilometer data used in this study is available in the following Zenodo repositories: https://doi.

org/10.5281/zenodo.11084027 (BLOOM; Abril-Gago et al., 2024a), https://doi.org/10.5281/zenodo.11085224 (BLOOM II, Abril-Gago et al., 2024b), https://doi.org/10.5281/zenodo.11085247 (SCARCE, Abril-Gago et al., 2024c). Readers may contact Jesús Abril-Gago (jabrilgago@ugr.es) and Juan Luis Guerrero-Rascado (rascado@ugr.es) before using the datasets. AERONET data is publicly available from the AERONET database (https://aeronet.gsfc.nasa.gov/).

References

Abel, C., Abdi, A.M., Tagesson, T., Horion, S., Fensholt, R., 2023. Contrasting ecosystem vegetation response in global drylands under drying and wetting conditions. Glob. Chang. Biol. 00, 1–16. https://doi.org/10.1111/gcb.16745.

Abril-Gago, J., Guerrero-Rascado, J.L., Costa, M.J., Bravo-Aranda, J.A., Sicard, M., Bermejo-Pantaleón, D., Bortoli, D., Granados-Muñoz, M.J., Rodríguez-Gómez, A., Muñoz-Porcar, C., Comerón, A., Ortiz-Amezcua, P., Salgueiro, V., Jiménez-Martín, M.M., Alados-Arboledas, L., 2022. Statistical validation of Aeolus L2A particle backscatter coefficient retrievals over ACTRIS/EARLINET stations on the Iberian Peninsula. Atmos. Chem. Phys. 22, 1425–1451. https://doi.org/10.5194/acp-22-1425-2022.

Abril-Gago, J., Ortiz-Amezcua, P., Bermejo-Pantaleón, D., Andújar-Maqueda, J., Bravo-Aranda, J.A., Granados-Muñoz, M.J., Navas-Guzmán, F., Alados-Arboledas, L., Foyo-Moreno, I., Guerrero-Rascado, J.L., 2023. Validation activities of Aeolus wind products on the southeastern Iberian Peninsula. Atmos. Chem. Phys. 23, 8453–8471. https://doi.org/10.5194/acp-23-8453-2023.

Abril-Gago, J., Andújar-Maqueda, J., Ortiz-Amezcua, P., Guerrero-Rascado, J.L., 2024a. BLOOM Campaign - Remote Sensing Datasets. Zenodo. https://doi.org/10.5281/zenodo.11084027.

Abril-Gago, J., Andújar-Maqueda, J., Ortiz-Amezcua, P., Guerrero-Rascado, J.L., 2024b. BLOOM II Campaign - Remote Sensing Datasets. Zenodo. https://doi.org/10.5281/zenodo.11085224.

Andújar-Maqueda, J., Ortiz-Amezcua, P. Cariñanos, P., Abril-Gago, J., De Linares, C., de Arruda Moreira, G., Bravo-Aranda, J.A., Granados-Muñoz, M.J., Alados-Arboledas, L., and Guerrero-Rascado, J.L., 2025. The Role of Atmospheric Boundary Layer Wind and Turbulence on Surface Pollen Levels. Agric. For. Meteorol., 371, 110584, doi: 10.1016/j.agrformet.2025.110584.

Abril-Gago, J., Andújar-Maqueda, J., Ortiz-Amezcua, P., Guerrero-Rascado, J.L., 2024c. SCARCE Campaign - Remote Sensing Datasets. Zenodo. https://doi.org/10.5281/zenodo.11085247.

Aguirre-Garcia, S.D., Aranda-Barranco, S., Nieto, H., Serrano-Ortiz, P., Sanchez-Canete, E.P., Guerrero-Rascado, J.L., 2021. Modelling actual evapotranspiration using a two source energy balance model with Sentinel imagery in herbaceous-free and herbaceous-cover Mediterranean olive orchards. Agric. For. Meteorol. 311, 108692. https://doi.org/10.1016/j.agrformet.2021.108692.

Alados, C.L., Pueyo, Y., Giner, M.L., Navarro, T., Escos, J., Barroso, F., Cabezudo, B., Emlen, J.M., 2003. Quantitative characterisation of the regressive ecological succession by fractal analysis of plant spatial patterns. Ecol. Model. 163, 1–17. https://doi.org/10.1016/S0304-3800(02)00294-6.

Ali, E., Cramer, W., Carnicer, J., Georgopoulou, E., Hilmi, N.J.M., Le Cozannet, G., Lionello, P., 2022. Cross-chapter paper 4: Mediterranean region. In: Pörtner, H.-O., Roberts, D.C., Tignor, M., Poloczanska, E.S., Mintenbeck, K., Alegría, A., Craig, M., Langsdorf, S., Löschke, S., Möller, V., Okem, A., Rama, B. (Eds.), Climate Change 2022: Impacts, Adaptation and Vulnerability. Contribution of Working Group II to the Sixth Assessment Report of the Intergovernmental Panel on Climate Change. Cambridge University Press, Cambridge, UK and New York, NY, USA, pp. 2233–2272. https://www.ipcc.ch/report/ar6/wg2/downloads/report/IPCC_AR6_WGII_CCP4.pdf.

Allen, R.J., Landuyt, W., Rumbold, S.T., 2016. An increase in aerosol burden and radiative effects in a warmer world. Nat. Clim. Chang. 6, 269–274. https://doi.org/10.1038/nclimate2827.

Aranda-Barranco, S., Serrano-Ortiz, P., Kowalski, A.S., Sánchez-Cañete, E.P., 2023. The temporary effect of weed-cover maintenance on transpiration and carbon assimilation of olive trees. Agric. For. Meteorol. 329, 109266. https://doi.org/10.1016/j.agrformet.2022.109266.

Aubinet, M., Grelle, A., Ibrom, A., Rannik, Ü., Moncrieff, J., Foken, T., Kowalski, A.S., Martin, P.H., Berbigier, P., Bernhofer, C., Clement, R., Elbers, J., Granier, S., Grünwald, T., Morgenstern, K., Pilegaard, K., Rebmann, C., Snijders, W., Valentini, R., Vesala, T., 1999. Estimates of the annual net carbon and water exchange of forests: the EUROFLUX methodology. Adv. Ecol. Res. 30, 113–175. https://doi.org/10.1016/S0065-2504(08)60018-5.

Baars, H., Seifert, P., Engelmann, R., Wandinger, U., 2017. Target categorization of aerosol and clouds by continuous multiwavelength-polarization lidar measurements. Atmos. Meas. Tech. 10, 3175–3201. https://doi.org/10.5194/amt-10-3175-2017.

Basart, S., Pérez, C., Nickovic, S., Cuevas, E., Baldasano, J.M., 2012. Development and evaluation of the BSC-DREAM8b dust regional model over Northern Africa, the Mediterranean and the Middle East. Tellus Ser. B Chem. Phys. Meteorol. 64 (1), 18539. https://doi.org/10.3402/tellusb.v64i0.18539.

Bergametti, G., Marticorena, B., Rajot, J.L., Foret, G., Alfaro, S.C., Laurent, B., 2018. Size-resolved dry deposition velocities of dust particles: in situ measurements and parameterizations testing. J. Geophys. Res. D: Atmos. 123, 11080–11099. https://doi.org/10.1029/2018JD028964.

Bhattachan, A., D'Odorico, P., 2014. Can land use intensification in the Mallee, Australia increase the supply of soluble iron to the Southern Ocean? Sci. Rep. 4, 6009. https://doi.org/10.1038/srep06009.

Bhattachan, A., D'Odorico, P., Baddock, M.C., Zobeck, T.M., Okin, G.S., Cassar, N., 2012. The Southern Kalahari: a potential new dust source in the Southern Hemisphere? Environ. Res. Lett. 7 (2), 024001. https://doi.org/10.1088/1748-9326/7/2/024001.

Bravo-Aranda, J.A., Titos, G., Granados-Muñoz, M.J., GuerreroRascado, J.L., Navas-Guzmán, F., Valenzuela, A., Lyamani, H., Olmo, F.J., Andrey, J., Alados-Arboledas, L., 2015. Study of mineral dust entrainment in the planetary boundary layer by lidar depolarisation technique. Tellus B 67, 26180. https://doi.org/10.3402/tellusb.v67.26180.

Capel Molina, J.J., 1995. Mapa pluviométrico de España peninsular y Baleares (en el período internacional 1961-1990). Investigaciones Geográficas 13, 29–46. https://doi.org/10.14198/INGEO1995.13.02.

Casquero-Vera, J.A., Lyamani, H., Titos, G., Moreira, G.D.A., Benavent-Oltra, J.A., Conte, M., Contini, D., Järvi, L., Olmo-Reyes, F.J., Alados-Arboledas, L., 2022. Aerosol number fluxes and concentrations over a southern european urban area. Atmos. Environ. 269. https://doi.org/10.1016/j.atmosenv.2021.118849.

Cazorla, A., Casquero-Vera, J.A., Román, R., Guerrero-Rascado, J.L., Toledano, C., Cachorro, V.E., Orza, J.A.G., Cancillo, M.L., Serrano, A., Titos, G., Pandolfi, M., Alastuey, A., Hanrieder, N., Alados-Arboledas, L., 2017. Near-real-time processing of a ceilometer network assisted with sun-photometer data: monitoring a dust outbreak over the Iberian Peninsula. Atmos. Chem. Phys. 17, 11861–11876. https://doi.org/10.5194/acp-17-11861-2017.

Chamberlain, A.C., Chadwick, R.C., 1953. Deposition of airborne radio-iodine vapour. Nucleonics 11, 22–25.

Chamizo, S., Serrano-Ortiz, P., López-Ballesteros, A., Sánchez-Cañete, E.P., Vicente-Vicente, J.L., Kowalski, A.S., 2017. Net Ecosystem CO2 Exchange in an Irrigated Olive Orchard of SE Spain: Influence of Weed Cover. Agric. Ecosyst. Environ. 239, 51–64. https://doi.org/10.1016/j.agee.2017.01.016.

Chu, H., Luo, X., Ouyang, Z., Chan, W.S., Dengel, S., Biraud, S.C., Torn, M.S., Metzger, S., Kumar, J., Arain, M.A., Arkebauer, T.J., Baldocchi, D., Bernacchi, C., Billesbach, D., Black, T.A., Blanken, P.D., Bohrer, G., Bracho, R., Brown, S., Brunsell, N.A., Chen, J., Chen, X., Clark, K., Desai, A.R., Duman, T., Durden, D., Fares, S., Forbrich, I., Gamon, J.A., Gough, C.M., Griffis, T., Helbig, M., Hollinger, D., Humphreys, E., Ikawa, H., Iwata, H., Ju, Y., Knowles, J.F., Knox, S.H., Kobayashi, H., Kolb, T., Law, B., Lee, X., Litvak, M., Liu, H., Munger, J.W., Noormets, A., Novick, K., Oberbauer, S.F., Oechel, W., Oikawa, P., Papuga, S.A., Pendall, E., Prajapati, P., Prueger, J., Quinton, W.L., Richardson, A.D., Russell, E.S., Scott, R.L., Starr, G., Staebler, R., Stoy, P.C., Stuart-Haëntjens, E., Sonnentag, O., Sullivan, R.C., Suyker, A., Ueyama, M., Vargas, R., Wood, J.D., Zona, D., 2021. Representativeness of Eddy-Covariance flux footprints for areas surrounding AmeriFlux sites. Agric. For. Meteorol. 301–302, 108350. https://doi.org/10.1016/J.AGRFORMET.2021.108350.

Cooper, D.I., Eichinger, W.E., Archuleta, J., Hipps, L., Kao, J., Leclerc, M.Y., Neale, C.M., Prueger, J., 2003. Spatial source-area analysis of three-dimensional moisture fields from lidar, eddy covariance, and a footprint model. Agric. For. Meteorol. 114 (3–4), 213–234. https://doi.org/10.1016/S0168-1923(02)00175-2.

de Bruine, M., Apituley, A., Donovan, D.P., Klein Baltink, H., de Haij, M.J., 2017. Pathfinder: applying graph theory to consistent tracking of daytime mixed layer height with backscatter lidar. Atmos. Meas. Tech. 10, 1893–1909. https://doi.org/10.5194/amt-10-1893-2017.

Deventer, M.J., von der Heyden, L., Lamprecht, C., Graus, M., Karl, T., Held, A., 2018. Aerosol particles during the Innsbruck Air Quality Study (INNAQS): fluxes of nucleation to accumulation mode particles in relation to selective urban tracers. Atmos. Environ. 190, 376–388. https://doi.org/10.1016/j.atmosenv.2018.04.043.

Donateo, A., Cava, D., Contini, D., 2017. A case study of the performance of different detrending methods in turbulent-flux estimation. Boundary-Layer Meteorol. 164, 19–37. https://doi.org/10.1007/s10546-017-0243-4.

Donateo, A., Pappaccogli, G., Famulari, D., Mazzola, M., Scoto, F., Decesari, S., 2023. Characterization of size-segregated particles' turbulent flux and deposition velocity by eddy correlation method at an Arctic site. Atmos. Chem. Phys. 23, 7425–7445. https://doi.org/10.5194/acp-23-7425-2023.

Dorsey, J.R., Nemitz, E., Gallagher, M.W., Fowler, D., Williams, P.I., Bower, K.N., Beswick, K.M., 2002. Direct measurements and parameterisation of aerosol flux, concentration and emission velocity above a city. Atmos. Environ. 36, 791–800. https://doi.org/10.1016/S1352-2310(01)00526-X.

Dubovik, O., Holben, B., Eck, T.F., Smirnov, A., Kaufman, Y.J., King, M.D., Tanré, D., Slutsker, I., 2002. Variability of absorption and optical properties of key aerosol types observed in worldwide locations. J. Atmos. Sci. 59, 590–608. https://doi.org/10.1175/1520-0469(2002)059%3C0590:VOAAOP%3E2.0.CO;2.

Dubovik, O., Sinyuk, A., Lapyonok, T., Holben, B.N., Mishchenko, M., Yang, P., Eck, T.F., Volten, H., Muñoz, O., Veihelmann, B., 2006. Application of spheroid models to account for aerosol particle nonsphericity in remote sensing of desert dust. J. Geophys. Res. Atmos. 111, D11208. https://doi.org/10.1029/2005JD006619.

Eichinger, W.E., Cooper, D.I., 2007. Using lidar remote sensing for spatially resolved measurements of evaporation and other meteorological parameters. Agron. J. 99, 255–271. https://doi.org/10.2134/agronj2005.0112S.

Eljamassi, A., Al-Najjar, H., Latif, M.A., Dweikat, A., Aljamal, M., 2023. Analysis of the climate change impact on the spatiotemporal drought in the Gaza region of the southeastern Mediterranean. Hydrol. Res. 54 (2), 165–188. https://doi.org/10.2166/nh.2022.083.

El-Kenawy, E.-S.M., Zerouali, B., Bailek, N., Bouchouich, K., Hassan, M.A., Almorox, J., Kuriqi, A., Eid, M., Ibrahim, A., 2022. Improved weighted ensemble learning for predicting the daily reference evapotranspiration under the semi-arid climate

conditions. Environ. Sci. Pollut. Res. 29, 81279–81299. https://doi.org/10.1007/s11356-022-21410-8.
Engelmann, R., Wandinger, U., Ansmann, A., Müller, D., Žeromskis, E., Althausen, D., Wehner, B., 2008. Lidar observations of the vertical aerosol flux in the planetary boundary layer. J. Atmos. Ocean. Technol. 25, 1296–1306. https://doi.org/10.1175/2007JTECHA967.1.
Farmer, D.K., Boedicker, E.K., DeBolt, H.M., 2021. Dry deposition of atmospheric aerosols: approaches, observations, and mechanisms. Annu. Rev. Phys. Chem. 72, 16.1–16.23. https://doi.org/10.1146/annurev-physchem-090519-034936.
Fernald, F.G., 1984. Analysis of atmospheric lidar observations: some comments. Appl. Opt. 23, 652–653. https://doi.org/10.1364/AO.23.000652.
Fernandes, R., Dupont, S., Lamaud, E., 2023. Experimental evidence of dust flux size distribution variation along two consecutive erosion seasons. Aeolian Res. 61, 100863. https://doi.org/10.1016/j.aeolia.2023.100863.
Foken, T., Wichura, B., 1996. Tools for quality assessment of surface-based flux measurements. Agric. For. Meteorol. 78, 83–105. https://doi.org/10.1016/0168-1923(95)02248-1.
Fuchs, N.A., 1964. The Mechanics of Aerosols. Macmillan, New York.
Gallagher, M.W., Beswick, K.M., Duyzer, J., Westrate, H., Choularton, T.W., Hummelshøj, P., 1997. Measurements of aerosol fluxes to speulderforest using a micrometeorological technique. Atmos. Environ. 31 (3), 359–373. https://doi.org/10.1016/S1352-2310(96)00057-X.
García-Valdecasas Ojeda, M., Gámiz-Fortis, S.R., Romero-Jiménez, E., Rosa-Cánovas, J. J., Yeste, P., Castro-Díez, Y., Esteban-Parra, M.J., 2021a. Projected changes in the Iberian Peninsula drought characteristics. Sci. Total Environ. 757, 143702. https://doi.org/10.1016/J.SCITOTENV.2020.143702.
García-Valdecasas Ojeda, M., Romero-Jiménez, E., Rosa-Cánovas, J.J., Yeste, P., Castro-Díez, Y., Esteban-Parra, M.J., Vicente-Serrano, S.M., Gámiz-Fortis, S.R., 2021b. Assessing future drought conditions over the Iberian Peninsula: the impact of using different periods to compute the SPEI. Atmosphere 12 (8), 980. https://doi.org/10.3390/atmos12080980.
Gash, J.H.C., Culf, A.D., 1996. Applying a linear detrend to eddy correlation data in realtime. Boundary-Layer Meteorol. 79, 301–306. https://doi.org/10.1007/BF00119443.
Gibert, F., Koch, G.J., Beyon, J.Y., Hilton, T.W., Davis, K.J., Andrews, A., Flamant, P.H., Singh, U.N., 2011. Can CO2 turbulent flux be measured by Lidar? A preliminary Study. J. Atmos. Ocean. Technol. 28, 365–377. https://doi.org/10.1175/2010JTECHA1446.1.
Gidarakou, M., Papayannis, A., Kokkalis, P., Evangeliou, N., Vratolis, S., Remoundaki, E., Groot Zwaaftink, C., Eckhardt, S., Veselovskii, I., Mylonaki, M., Argyrouli, A., Eleftheriadis, K., Solomos, S., Gini, M.I., 2024. Optical and microphysical properties of the aerosols during a rare event of biomass-burning mixed with polluted dust. Atmosphere 15 (2), 190. https://doi.org/10.3390/atmos15020190.
Giez, A., Ehret, G., Schwiesow, R.L., Davis, K.J., Lenschow, D.H., 1999. Water vapor flux measurements from ground-based vertically pointed water vapor differential absorption and Doppler lidars. J. Atmos. Ocean. Technol. 16, 237–250. https://doi.org/10.1175/1520-0426(1999)016<0237:WVFMFG>2.0.CO;2.
Goto, S., Vassilicos, J.C., 2016. Unsteady turbulence cascades. Phys. Rev. E 94, 053108. https://doi.org/10.1103/PhysRevE.94.053108.
Granados-Muñoz, M.J., Bravo-Aranda, J.A., Baumgardner, D., Guerrero-Rascado, J.L., Pérez-Ramírez, D., Navas-Guzmán, F., Veselovskii, I., Lyamani, H., Valenzuela, A., Olmo, F.J., Titos, G., Andrey, J., Chaikovsky, A., Dubovik, O., Gil-Ojeda, M., Alados-Arboledas, L., 2016. A comparative study of aerosol microphysical properties retrieved from ground-based remote sensing and aircraft in situ measurements during a Saharan dust event. Atmos. Meas. Tech. 9, 1113–1133. https://doi.org/10.5194/amt9-1113-2016.
Guerrero-Rascado, J.L., Ruiz, B., Alados-Arboledas, L., 2008. Multispectral Lidar characterization of the vertical structure of Saharan dust aerosol over southern Spain. Atmos. Environ. 42, 2668–2681. https://doi.org/10.1016/j.atmosenv.2007.12.062.
Guerrero-Rascado, J.L., Olmo, F.J., Avilés-Rodríguez, I., NavasGuzmán, F., Pérez-Ramírez, D., Lyamani, H., Alados Arboledas, L., 2009. Extreme Saharan dust event over the southern Iberian Peninsula in september 2007: active and passive remote sensing from surface and satellite. Atmos. Chem. Phys. 9, 8453–8469. https://doi.org/10.5194/acp-9-8453-2009.
Hari, P., Nikinmaa, E., Pohja, T., Siivola, E., Bäck, J., Vesala, T., Kulmala, M., 2013. Station for measuring Ecosystem-Atmosphere Relations: SMEAR. In: Hari, P., Heliövaara, K., Kulmala, L. (Eds.), Physical and Physiological Forest Ecology. Springer, Dordrecht. https://doi.org/10.1007/978-94-007-5603-8_9.
HMSO, 1962. Weather in the Mediterranean I: General Meteorology, 2nd ed. Her Majesty's Stationery Office. 362 p.
Holben, B.N., Eck, T.F., Slutsker, I., Tanré, D., Buis, J.P., Setzer, A., Vermote, E., Reagan, J.A., Kaufman, Y.J., Nakajima, T., Lavenu, F., Jankowiak, I., Smirnov, A., 1998. AERONET - a federated instrument network and data archive for aerosol characterization. Remote Sens. Environ. 66, 1–16. https://doi.org/10.1016/S0034-4257(98)00031-5.
IPCC, 2001. Climate change 2001: the scientific basis. In: Houghton, J.T., Ding, Y., Griggs, D.J., Noguer, M., van der Linden, P.J., Dai, X., Maskell, K., Johnson, C.A. (Eds.), Contribution of Working Group I to the Third Assessment Report of the Intergovernmental Panel on Climate Change. Cambridge University Press, Cambridge, United Kingdom and New York, NY, USA, 881 pp. https://www.ipcc.ch/site/assets/uploads/2018/03/WGI_TAR_full_report.pdf.
IPCC, 2007. Climate change 2007: the physical science basis. In: Solomon, S., Qin, D., Manning, M., Chen, Z., Marquis, M., Averyt, K.B., Tignor, M., Miller, H.L. (Eds.), Contribution of Working Group I to the Fourth Assessment Report of the Intergovernmental Panel on Climate Change. Cambridge University Press, Cambridge, United Kingdom and New York, NY, USA, 996 pp. https://www.ipcc.ch/site/assets/uploads/2018/05/ar4_wg1_full_report-1.pdf.
IPCC, 2013. Climate change 2013: the physical science basis. In: Stocker, T.F., Qin, D., Plattner, G.-K., Tignor, M., Allen, S.K., Boschung, J., Nauels, A., Xia, Y., Bex, V., Midgley, P.M. (Eds.), Contribution of Working Group I to the Fifth Assessment Report of the Intergovernmental Panel on Climate Change. Cambridge University Press, Cambridge, United Kingdom and New York, NY, USA. https://doi.org/10.1017/CBO9781107415324, 1535 pp.
IPCC, 2021. Climate change 2021: the physical science basis. In: Masson-Delmotte, V., Zhai, P., Pirani, A., Connors, S.L., Péan, C., Berger, S., Caud, N., Chen, Y., Goldfarb, L., Gomis, M.I., Huang, M., Leitzell, K., Lonnoy, E., Matthews, J.B.R., Maycock, T.K., Waterfield, T., Yelekçi, O., Yu, R., Zhou, B. (Eds.), Contribution of Working Group I to the Sixth Assessment Report of the Intergovernmental Panel on Climate Change. Cambridge University Press, Cambridge, United Kingdom and New York, NY, USA. https://doi.org/10.1017/9781009157896, 2391 pp.
Ishizuka, M., Mikami, M., Leys, J., Yamada, Y., Heidenreich, S., Shao, Y., McTainsh, G.H., 2008. Effects of soil moisture and dried raindroplet crust on saltation and dust emission. J. Geophys. Res. 113, D24212. https://doi.org/10.1029/2008JD009955.
Järvi, L., Rannik, Ü., Mammarella, I., Sogachev, A., Aalto, P.P., Keronen, P., Siivola, E., Kulmala, M., Vesala, T., 2009. Annual particle flux observations over a heterogeneous urban area. Atmos. Chem. Phys. 9, 7847–7856. https://doi.org/10.5194/acp-9-7847-2009.
Kaimal, J.C., Wyngaard, J.C., Izumi, Y., Coté, O.R., 1972. Spectral characteristics of surface-layer turbulence. Q. J. R. Meteorol. Soc. 98, 563–589. https://doi.org/10.1002/qj.49709841707.
Karasewicz, M., Wacławczyk, M., Ortiz-Amezcua, P., Janicka, Ł., Poczta, P., Kassar Borges, C., Stachlewska, I.S., 2024. Investigation of non-equilibrium turbulence decay in the atmospheric boundary layer using Doppler lidar measurements. Atmos. Chem. Phys. 24, 13231–13251. https://doi.org/10.5194/acp-24-13231-2024.
Klett, J.D., 1981. Stable analytic inversion solution for processing lidar returns. Appl. Opt. 20, 211–220. https://doi.org/10.1364/AO.20.000211.
Kljun, N., Calanca, P., Rotach, M.W., Schmid, H.P., 2015. A simple two-dimensional parameterisation for Flux Footprint Prediction (FFP). Geosci. Model Dev. 8, 3695–3713. https://doi.org/10.5194/gmd-8-3695-2015.
Kolmogorov, A.N., 1941. Dissipation of energy in locally isotropic turbulence. Dokl. Akad. Nauk SSSR 32, 16–18.
Kotthaus, S., Haeffelin, M., Drouin, M.-A., Dupont, J.-C., Grimmond, S., Haefele, A., Hervo, M., Poltera, Y., Wiegner, M., 2020. Tailored algorithms for the detection of the atmospheric boundary layer height from common automatic lidars and ceilometers (ALC). Remote Sens. 12, 3259. https://doi.org/10.3390/rs12193259.
Kowalski, A., 2001. Deliquescence induces eddy covariance and estimable dry deposition errors. Atmos. Environ. 35, 4843–4851. https://doi.org/10.1016/S1352-2310(01)00270-9.
Kowalski, A.S., 2023. The flux you say?: comments on "The Integrated Carbon Observation System in Europe". Bull. Amer. Meteor. Soc. 104, 949–952. https://doi.org/10.1175/BAMS-D-22-0274.1.
Kowalski, A.S., Abril-Gago, J., 2025. Exploring unresolved inquiries regarding the meaning of Reynolds averaging and decomposition: a review. Agric. For. Meteorol. 362, 110364. https://doi.org/10.1016/j.agrformet.2024.110364.
Kristensen, L., Mann, J., Oncley, S.P., Wyngaard, J.C., 1997. How close is close enough when measuring scalar fluxes with displaced sensors? J. Atmos. Ocean. Technol. 14 (4), 814–821. https://doi.org/10.1175/1520-0426(1997)014<0814:HCICEW>2.0.CO;2.
Lamaud, E., Chapuis, A., Fontan, J., Serie, E., 1994. Measurements and parameterization of aerosol dry deposition in a semi-arid area. Atmos. Environ. 28, 2461–2471. https://doi.org/10.1016/1352-2310(94)90397-2.
Leclerc, M.Y., Foken, T., 2014. Footprints in Micrometeorology and Ecology Volume 239. Springer, Berlin. https://doi.org/10.1007/978-3-642-54545-0.
Longley, I.D., Gallagher, M.W., Dorsey, J.R., Flynn, M., Bower, K.N., Allan, J.D., 2004. Street canyon aerosol pollutant transport measurements. Sci. Total Environ. 334–335, 327–336. https://doi.org/10.1016/j.scitotenv.2004.04.072.
López-Ballesteros, A., Oyonarte, C., Kowalski, A.S., Serrano-Ortiz, P., Sánchez-Cañete, E. P., Moya, M.R., Domingo, F., 2018. Can land degradation drive differences in the C exchange of two similar semiarid ecosystems? Biogeosciences 15, 263–278. https://doi.org/10.5194/bg-15-263-2018.
López-Cayuela, M.A., Herreras-Giralda, M., Córdoba-Jabonero, C., Lopatin, A., Dubovik, O., Guerrero-Rascado, J.L., 2021. Vertical assessment of the mineral dust optical and microphysical properties as retrieved from the synergy between polarized micro-pulse lidar and sun/sky photometer observations using GRASP code. Atmos. Res. 264. https://doi.org/10.1016/j.atmosres.2021.105818.
López-Cayuela, M.Á., Córdoba-Jabonero, C., Bermejo-Pantaleón, D., Sicard, M., Salgueiro, V., Molero, F., Carvajal-Pérez, C.V., Granados-Muñoz, M.J., Comerón, A., Couto, F.T., Barragán, R., Zorzano, M.-P., Bravo-Aranda, J.A., Muñoz-Porcar, C., Costa, M.J., Artíñano, B., Rodríguez-Gómez, A., Bortoli, D., Pujadas, M., Abril-Gago, J., Alados-Arboledas, L., Guerrero-Rascado, J.L., 2023. Vertical characterization of fine and coarse dust particles during an intense Saharan dust outbreak over the Iberian Peninsula in springtime 2021. Atmos. Chem. Phys. 23, 143–161. https://doi.org/10.5194/acp-23-143-2023.
Mandija, F., Guerrero-Rascado, J.L., Lyamani, H., Granados-Muñoz, M.J., Alados-Arboledas, L., 2016. Synergic estimation of columnar integrated aerosol properties and their vertical resolved profiles in respect to the scenarios of dust intrusions over Granada. Atmos. Environ. 145, 439–454. https://doi.org/10.1016/j.atmosenv.2016.09.045.
Manninen, A.J., 2019. HALO Lidar Toolbox. Github. https://github.com/manninenaj/HALO_lidar_toolbox.

Manninen, A.J., O'Connor, E.J., Vakkari, V., Petäjä, T., 2016. A generalised background correction algorithm for a Halo Doppler lidar and its application to data from Finland. Atmos. Meas. Tech. 9, 817–827. https://doi.org/10.5194/amt-9-817-2016.

Manninen, A.J., Marke, T., Tuononen, M.J., O'Connor, E.J., 2018. Atmospheric boundary layer classification with Doppler lidar. J. Geophys. Res. D: Atmos. 123, 8172–8189. https://doi.org/10.1029/2017JD028169.

Masseroni, D., Corbari, C., Mancini, M., 2014. Limitations and improvements of the energy balance closure with reference to experimental data measured over a maize field. Atmósfera 27 (4), 335–352. https://doi.org/10.1016/S0187-6236(14)70033-5.

Matthews, B., Schume, H., 2022. Tall tower eddy covariance measurements of CO2 fluxes in Vienna, Austria. Atmos. Environ. 274, 118941. https://doi.org/10.1016/j.atmosenv.2022.118941.

Mirzabaev, A., Wu, J., Evans, J., García-Oliva, F., Hussein, I.A.G., Iqbal, M.H., Kimutai, J., Knowles, T., Meza, F., Nedjraoui, D., Tena, F., Türkeş, M., Vázquez, R.J., Weltz, M., 2019. Desertification. In: Shukla, P.R., Skea, J., Buendia, E. Calvo, Masson-Delmotte, V., Pörtner, H.-O., Roberts, D.C., Zhai, P., Slade, R., Connors, S., van Diemen, R., Ferrat, M., Haughey, E., Luz, S., Neogi, S., Pathak, M., Petzold, J., Pereira, J. Portugal, Vyas, P., Huntley, E., Kissick, K., Belkacemi, M., Malley, J. (Eds.), Climate Change and Land: An IPCC Special Report on Climate Change, Desertification, Land Degradation, Sustainable Land Management, Food Security, and Greenhouse Gas Fluxes in Terrestrial Ecosystems. https://doi.org/10.1017/9781009157988.005.

Mirzabaev, A., Stringer, L.C., Benjaminsen, T.A., Gonzalez, P., Harris, R., Jafari, M., Stevens, N., Tirado, C.M., Zakieldeen, S., 2022. Cross-chapter paper 3: deserts, semiarid areas and desertification. In: Pörtner, H.-O., Roberts, D.C., Tignor, M., Poloczanska, E.S., Mintenbeck, K., Alegría, A., Craig, M., Langsdorf, S., Löschke, S., Möller, V., Okem, A., Rama, B. (Eds.), Climate Change 2022: Impacts, Adaptation and Vulnerability. Contribution of Working Group II to the Sixth Assessment Report of the Intergovernmental Panel on Climate Change. Cambridge University Press, Cambridge, UK and New York, NY, USA, pp. 2195–2231. https://www.ipcc.ch/report/ar6/wg2/downloads/report/IPCC_AR6_WGII_CCP3.pdf.

Molinero-García, A., Martín-García, J.M., Fernández-González, M.V., Delgado, R., 2022. Provenance fingerprints of atmospheric dust collected at Granada city (Southern Iberian Peninsula). Evidence from quartz grains. CATENA 208, 105738. https://doi.org/10.1016/j.catena.2021.105738.

Moya, M.R., Sánchez-Cañete, E.P., Vargas, R., López-Ballesteros, A., Oyonarte, C., Kowalski, A.S., Serrano-Ortiz, P., Domingo, F., 2019. CO_2 dynamics are strongly influenced by low frequency atmospheric pressure changes in semiarid grasslands. J. Geophys. Res. Biogeosci. 124, 902–917. https://doi.org/10.1029/2018JG004961.

Nilsson, E.D., Rannik, Ü., Kumala, M., Buzorius, G., O'dowd, C.D., 2001. Effects of continental boundary layer evolution, convection, turbulence and entrainment, on aerosol formation. Tellus Ser. B Chem. Phys. Meteorol. 53 (4), 441–461. https://doi.org/10.3402/tellusb.v53i4.16617.

Obligado, M., Vassilicos, J.C., 2019. The non-equilibrium part of the inertial range in decaying homogeneous turbulence. EPL 127, 64004. https://doi.org/10.1209/0295-5075/127/64004.

O'Connor, E.J., Illingworth, A.J., Brooks, I.M., Westbrook, C.D., Hogan, R.J., Davies, F., Brooks, B.J., 2010. A method for estimating the turbulent kinetic energy dissipation rate from a vertically pointing Doppler lidar, and independent evaluation from balloon-borne in situ measurements. J. Atmos. Ocean. Technol. 27, 1652–1664. https://doi.org/10.1175/2010JTECHA1455.1.

Ortiz-Amezcua, P., 2023. Remote Sensing Aerosol Flux Toolbox. Zenodo. https://doi.org/10.5281/zenodo.8394916.

Ortiz-Amezcua, P., Martínez-Herrera, A., Manninen, A.J., Pentikäinen, P.P., O'Connor, E. J., Guerrero-Rascado, J.L., Alados-Arboledas, L., 2022a. Wind and turbulence statistics in the urban boundary layer over a mountain–valley system in Granada, Spain. Remote Sens. 14, 2321. https://doi.org/10.3390/rs14102321.

Ortiz-Amezcua, P., Andújar-Maqueda, J., Manninen, A.J., Pentikäinen, P., O'Connor, E. J., Stachlewska, I.S., de Arruda Moreira, G., Benavent-Oltra, J.A., Casquero-Vera, J. A., Poczta, P., Wang, D., Harenda, K.M., Chojnicki, B.H., Szczepanik, D.M., Janicka, Ł., Schüttemeyer, D., Alados-Arboledas, L., Guerrero-Rascado, J.L., 2022b. Dynamics of the atmospheric boundary layer over two middle-latitude rural sites with Doppler lidar. Atmos. Res. 280, 106434. https://doi.org/10.1016/j.atmosres.2022.106434.

Pal, S., Behrendt, A., Wulfmeyer, V., 2010. Elastic-backscatter-lidarbased characterization of the convective boundary layer and investigation of related statistics. Ann. Geophys. 28, 825–847. https://doi.org/10.5194/angeo-28-825-2010.

Papanikolaou, C.-A., Papayannis, A., Gidarakou, M., Abdullaev, S.F., Ajtai, N., Baars, H., Balis, D., Bortoli, D., Bravo–Aranda, J.A., Collaud Coen, M., de Rosa, B., Dionisi, D., Eleftheratos, K., Engelmann, R., Floutsi, A.A., Abril-Gago, J., Goloub, P., Giuliano, G., Gumà Claramunt, P., Hofer, J., Hu, Q., Komppula, M., Marinou, E., Martucci, G., Mattis, I., Michailidis, K., Muñoz–Porcar, C., Mylonaki, M., Mytilinaios, M., Nicolae, D., Rodríguez–Gómez, A., Salgueiro, V., Shang, X., Stachlewska, I.S., Ștefănie, H.I., Szczepanik, D.M., Trickl, T., Vogelmann, H., Artemis Voudouri, K., 2024. Large-scale network-based observations of a Saharan dust event across the European continent in spring 2022. Remote Sens. 16, 3350. https://doi.org/10.3390/rs16173350.

Pappaccogli, G., Famulari, D., Donateo, A., 2022. Impact of filtering methods on ultrafine particles turbulent fluxes by eddy covariance. Atmos. Environ. 285, 119237. https://doi.org/10.1016/j.atmosenv.2022.119237.

Pentikäinen, P., O'Connor, E.J., Manninen, A.J., Ortiz-Amezcua, P., 2020. Methodology for deriving the telescope focus function and its uncertainty for a heterodyne pulsed Doppler lidar. Atmos. Meas. Tech. 13, 2849–2863. https://doi.org/10.5194/amt-13-2849-2020.

Petters, M.D., Pujiastuti, T., Rasheeda Satheesh, A., Kasparoglu, S., Sutherland, B., Meskhidze, N., 2024. Wind-driven emissions of coarse-mode particles in an urban environment. Atmos. Chem. Phys. 24, 745–762. https://doi.org/10.5194/acp-24-745-2024.

Poltera, Y., Martucci, G., Collaud Coen, M., Hervo, M., Emmenegger, L., Henne, S., Brunner, D., Haefele, A., 2017. PathfinderTURB: an automatic boundary layer algorithm. Development, validation and application to study the impact on in situ measurements at the Jungfraujoch. Atmos. Chem. Phys. 17, 10051–10070. https://doi.org/10.5194/acp-17-10051-2017.

Pryor, S.C., 2006. Size resolved particle deposition velocities of sub-100 nm diameter particles over a forest. Atmos. Environ. 40, 6192–6200. https://doi.org/10.1016/j.atmosenv.2006.04.066.

Pryor, S.C., Larsen, S.E., SØrensen, L.L., Barthelmie, R.J., Grönholm, T., Kulmala, M., Launiainen, S., Rannik, Ü., Vesala, T., 2007. Particle fluxes over forests: analysis of flux methods and functional dependencies. J. Geophys. Res. 112. https://doi.org/10.1029/2006JD008066.

Pryor, S.C., Gallagher, M., Sievering, H., Larsen, S.E., Barthelmie, R.J., Birsan, F., Nemitz, E., Rinne, J., Kulmala, M., Grönholm, T., Taipale, R., Vesala, T., 2008. A review of measurement and modelling results of particle atmosphere-surface exchange. Tellus Ser. B Chem. Phys. Meteorol. 60 (1), 42–75. https://doi.org/10.1111/j.1600-0889.2007.00298.x.

Pryor, S.C., Barthelmie, R.J., Larsen, S.E., Sørensen, L.L., 2017. Ultrafine particle number fluxes over and in a deciduous forest. J. Geophys. Res. Atmos. 122, 405–422. https://doi.org/10.1002/2016JD025854.

Rannik, Ü., Mammarella, I., Aalto, P., Keronen, P., Vesala, T., Kulmala, M., 2009. Long-term aerosol particle flux observations part I: uncertainties and time-average statistics. Atmos. Environ. 43 (21), 3431–3439. https://doi.org/10.1016/j.atmosenv.2009.02.049.

Rasheeda Satheesh, A., Petters, M.D., Meskhidze, N., 2024. Aerosol vertical turbulent mass flux retrievals through novel remote sensing algorithm. J. Geophys. Res. Atmos. 129, e2023JD040322. https://doi.org/10.1029/2023JD040322.

Salgueiro, V., Cerqueira, M., Monteiro, A., Alves, C., Rafael, S., Borrego, C., Pio, C., 2020. Annual and seasonal variability of greenhouse gases fluxes over coastal urban and suburban areas in Portugal: measurements and source partitioning. Atmos. Environ. 223, 117204. https://doi.org/10.1016/j.atmosenv.2019.117204.

Salgueiro, V., Costa, M.J., Guerrero-Rascado, J.G., Couto, F.T., Bortoli, D., 2021. Characterization of forest fire and saharan desert dust aerosols over South-Western Europe using a multi-wavelength raman lidar and sun-photometer. Atmos. Environ. 252. https://doi.org/10.1016/j.atmosenv.2021.118346.

Salgueiro, V., Guerrero-Rascado, J.L., Costa, M.J., Román, R., Cazorla, A., Serrano, A., Molero, F., Sicard, M., Córdoba-Jabonero, C., Bortoli, D., Comerón, A., Couto, F.T., López-Cayuela, M.-Á., Pérez-Ramírez, D., Potes, M., Muñiz-Rosado, J.A., Barragán, R., Oliveira, D.C.F.S., Abril-Gago, J., González, R., Gíl-Díaz, C., Foyo-Moreno, I., Muñoz-Porcar, C., Granados-Muñoz, M.J., Rodríguez-Gómez, A., Herreras-Giralda, M., Bravo-Aranda, J.A., Carvajal-Pérez, C.V., Barreto, A., Alados-Arboledas, L., 2023. Characterization of Tajogaite volcanic plumes detected over the Iberian Peninsula from a set of satellite and ground-based remote sensing instrumentation. Remote Sens. Environ. 295, 113684. https://doi.org/10.1016/j.rse.2023.113684.

Sánchez-Cañete, E.P., Oyonarte, C., Serrano-Ortiz, P., Curiel Yuste, J., Pérez-Priego, O., Domingo, F., Kowalski, A.S., 2016. Winds induce CO2 exchange with the atmosphere and vadose zone transport in a karstic ecosystem. J. Geophys. Res. Biogeosci. 121, 2049–2063. https://doi.org/10.1002/2016JG003500.

Schmid, H.P., 1997. Experimental design for flux measurements: matching scales of observations and fluxes. Agric. For. Meteorol. 87, 179–200. https://doi.org/10.1016/S0168-1923(97)00011-7.

Schuepp, P.H., Leclerc, M.Y., Macpherson, J.I., Desjardins, R.L., 1990. Footprint prediction of scalar fluxes from analytical solutions of the diffusion equation. Bound.-Layer Meteor. 50, 355–373. https://doi.org/10.1175/JTECH1911.1.

Senff, C., Bösenberg, J., Peters, G., 1994. Measurement of water vapor flux profiles in the convective boundary layer with lidar and radar-RASS. J. Atmos. Ocean. Technol. 11 (1), 85–93. https://doi.org/10.1175/1520-0426(1994)011<0085:MOWVFP>2.0.CO;2.

Serrano-Ortiz, P., Marañón-Jiménez, S., Reverter, B.R., Sánchez-Cañete, E.P., Castro, J., Zamora, R., Kowalski, A.S., 2011. Post-fire salvage logging reduces carbon sequestration in Mediterranean coniferous forest. For. Ecol. Manag. 262, 2287–2296. https://doi.org/10.1016/j.foreco.2011.08.023.

Serrano-Ortiz, P., Aranda-Barranco, S., López-Ballesteros, A., Lopez-Canfin, C., Sánchez-Cañete, E.P., Meijide, A., Kowalski, A.S., 2020. Transition period between vegetation growth and senescence controlling interannual variability of C fluxes in a Mediterranean reed wetland. J. Geophys. Res. Biogeosci. 125, e2019JG005169. https://doi.org/10.1029/2019JG005169.

Shin, S.-K., Tesche, M., Noh, Y., Müller, D., 2019. Aerosol-type classification based on AERONET version 3 inversion products. Atmos. Meas. Tech. 12, 3789–3803. https://doi.org/10.5194/amt-12-3789-2019.

Sievering, H., 1987. Small particle dry deposition under high wind speed conditions: eddy flux measurements at the Boulder Atmospheric Observatory. Atmos. Environ. 21, 2179–2185. https://doi.org/10.1016/0004-6981(87)90350-7.

Spinoni, J., Vogt, J.V., Naumann, G., Barbosa, P., Dosio, A., 2018. Will drought events become more frequent and severe in Europe? Int. J. Climatol. 38, 1718–1736. https://doi.org/10.1002/joc.5291.

Steiros, K., 2022. Turbulence near initial conditions. Phys. Rev. Fluids 10, 104607. https://doi.org/10.1103/PhysRevFluids.7.104607.

Straaten, A., Weber, S., 2021. Measurement report: three years of size-resolved eddy-covariance particle number flux measurements in an urban environment. Atmos. Chem. Phys. 21, 18707–18726. https://doi.org/10.5194/acp-21-18707-2021.

Stull, R.B., 1988. An Introduction to Boundary Layer Meteorology. Springer. https://doi.org/10.1007/978-94-009-3027-8.

Tegen, I., Schepanski, K., 2018. Climate feedback on aerosol emission and atmospheric concentrations. Curr. Clim. Chang. Rep. 4, 1–10. https://doi.org/10.1007/s40641-018-0086-1.

Vakkari, V., Manninen, A.J., O'Connor, E.J., Schween, J.H., Van Zyl, P.G., Marinou, E., 2019. A novel post-processing algorithm for Halo Doppler lidars. Atmos. Meas. Tech. 12 (2), 839–852. https://doi.org/10.5194/amt-12-839-2019.

Vong, R.J., Vickers, D., Covert, D.S., 2004. Eddy correlation measurements of aerosol deposition to grass. Tellus Ser. B Chem. Phys. Meteorol. 105–117. https://doi.org/10.1111/j.1600-0889.2004.00098.x.

Wacławczyk, T., 2021. Modeling of non-equilibrium effects in intermittency region between two phases. Int. J. Multiphase Flow 134, 103459. https://doi.org/10.1016/j.ijmultiphaseflow.2020.103459.

Wacławczyk, M., Nowak, J.L., Siebert, H., Malinowski, S.P., 2022. Detecting non-equilibrium states in atmospheric turbulence. J. Atmos. Sci. 79, 2757–2772. https://doi.org/10.1175/JAS-D-22-0028.1.

Wandinger, U., 2005. Introduction to lidar. In: Weitkamp, C. (Ed.), Lidar-Range-Resolved Optical Remote Sensing of the Atmosphere. Springer, New York, pp. 1–18.

Wang, W., Davis, K.J., Ricciuto, D.M., Butler, M.P., 2006. An approximate footprint model for flux measurements in the convective boundary layer. J. Atmos. Ocean. Technol. 23, 1384–1394. https://doi.org/10.1175/JTECH1911.1.

Wang, X., Dai, G., Wu, S., Sun, K., Song, X., Chen, W., Li, R., Yin, J., Wang, X., 2021. Retrieval and calculation of vertical aerosol mass fluxes by a coherent Doppler lidar and a sun photometer. Remote Sens. 13, 3259. https://doi.org/10.3390/rs13163259.

Webb, N.P., Pierre, C., 2018. Quantifying Anthropogenic Dust Emissions. Earths. Future 6 (2), 286–295. https://doi.org/10.1002/2017EF000766.

Webb, E.K., Pearman, G., Leuning, R., 1980. Correction of flux measurements for density effects due to heat and water vapour transfer. Q. J. R. Meteorol. Soc. 106, 85–100. https://doi.org/10.1002/qj.49710644707.

Webb, N.P., LeGrand, S.L., Cooper, B.F., Courtright, E.M., Edwards, B.L., Felt, C., Van Zee, J.W., Ziegler, N.P., 2021. Size distribution of mineral dust emissions from sparsely vegetated and supply-limited dryland soils. J. Geophys. Res. D: Atmos. 126, e2021JD035478. https://doi.org/10.1029/2021JD035478.

Wesely, M.L., Hicks, B.B., Dannevick, W.P., Frissela, S., Hauser, R.B., 1977. An eddy correlation measurement of particle deposition from the atmosphere. Atmos. Environ. 11, 561–563. https://doi.org/10.1016/0004-6981(77)90076-2.

Westphal, D.L., Curtis, C.A., Liu, M., Walker, A.L., 2009. Operational aerosol and dust storm forecasting, in WMO/GEO expert meeting on an international sand and dust storm warning system. IOP Conf. Ser.: Earth Environ. Sci 7, 012007, 15. https://doi.org/10.1088/1755-1307/7/1/012007.

Zdruli, P., 2011. Desertification in the Mediterranean Region. European Institute of the Mediterranean, Girona, Barcelona, 250–255 pp.